Norwegian University
of Life Sciences

Master's Thesis 2020 30 ECTS
Faculty of Science and Technology

Parametric study of the behavior of steel cellular beams with various web opening diameters

Abdimalik Sheikh Muhumed
Structural Engineering and Architecture

Preface

This Master Thesis is written in the spring semester of 2020 at the Faculty of Science and Technology at the Norwegian University of Life Sciences (NMBU).

The aim of this thesis is to analyze the behavior of steel cellular beams with different web opening diameters. Several parameters are varied to find out the contribution of each parameter to the overall strength of the perforated steel beam. It has been a challenging task to familiarize with the ANSYS software package that has been used for the numerical simulations, however I have learned a lot during this useful process.

Acknowledgement

I am greatly indebted to my supervisor, Themistoklis Tsalkatidis, Associate Professor at the Norwegian University of Life Sciences for his support and continuous guidance during my research.

I would also like to thank my beloved family for their patience and understanding throughout the period required for the completion of the thesis.

Abstract

Steel cellular beams are beams with circular web openings along their length which are fabricated from hot rolled steel sections. One of the main advantages of building with cellular beams is the possibility of passing electric wires and ventilation systems through the depth of the beam, which reduces the height of floors. They are mainly used as roof and floor beams to achieve long spans in excess of 12m.

The objective of this master thesis is to investigate the effect of different parameters on the strength of the web-post. Many previous experimental and numerical analyses have been conducted on cellular beams; however, the focus of the thesis is placed on three parameters, namely the diameter of the web opening, the thickness of the flanges and the thickness of the web.

Experimental results from testing series carried out in a previous research paper have been used to validate the proposed three-dimensional finite element model that have been created using ANSYS Workbench. In order to determine the effect of these parametric changes, 12 cases have been studied and an optimal case design is proposed in this thesis.

The base model is a universal beam section UB457x152x52 with top and bottom flange thickness of 10.9mm, web thickness of 7.6mm and web-opening diameter of 315mm. After analyzing a total number of 12 cases, it is concluded that case 3a is the optimal case with top and bottom flange thickness of 10.9mm, web thickness of 11.4mm and web opening diameter of 315mm. The web-post shear capacity increased by 45.5% with this parametric combination.

Keywords:

Steel cellular beams, finite element analysis, parametric study, web opening diameter, web-post

Sammendrag

Stål cellulære bjelker er bjelker med sirkulære stegåpninger langs deres lengde som er produsert av varmvalsede stålseksjoner. En av hovedfordelene med å bygge med cellulære bjelker er muligheten for å føre elektriske ledninger og ventilasjonssystemer gjennom dybden på bjelken, noe som reduserer etasjehøyden. De brukes hovedsakelig som tak- og gulvbjelker for å oppnå lange spenn over 12m.

Målet med denne masteroppgaven er å undersøke effekten av forskjellige parametere på styrken til steginnlegget. Mange tidligere eksperimentelle og numeriske analyser er blitt utført på cellulære bjelker, men fokuset for denne oppgaven er plassert på tre parametere, nemlig diameteren til stegåpningen, tykkelsen på flensene og tykkelsen på steget.

Eksperimentelle resultater fra testserier utført i en tidligere forskningsoppgave har blitt brukt for å validere den foreslåtte tredimensjonal elementmodellen som er laget i ANSYS Workbench. For å bestemme effekten av disse parametriske endringene er 12 tilfeller blitt studert og en optimal utforming foreslås i denne oppgaven.

Basismodellen er en bjelketverrsnitt UB457x152x52 med topp- og bunnflensetykkelse på 10,9mm, stegtykkelse på 7,6mm og stegåpningsdiameter på 315mm. Etter å ha analysert et totalt antall på 12 tilfeller, konkluderes det med at tilfelle 3a er det optimale tilfellet med topp- og bunnflensetykkelse på 10,9mm, stegtykkelse på 11,4mm og stegåpningens diameter på 315mm. Skjærkapasiteten til steginnlegget økte med 45,5% med denne parametriske kombinasjonen.

Nøkkelord:

Stål cellulære bjelker, elementmetode, parametrisk undersøkelse, stegåpningsdiameter, steginnlegg

Table of Contents

List of Figures

List of Tables

Symbols

A_v	–	Shear area
d_0	–	Web opening diameter
E	–	Modulus of elasticity
f_y	–	Yield strength
I	–	Moment of inertia
I_w	–	Warping stiffness
k and k_w	–	Effective length factors
L	–	Distance between lateral braced section
M_{Ed}	–	Design bending moment
$M_{c,Rd}$	–	Bending moment resistance
$M_{y,Ed}$	–	Design bending moment, y-y axis
$M_{z,Ed}$	–	Design bending moment, z-z axis
$M_{y,Rd}$	–	Design bending moment resistance, y-y axis
$M_{z,Rd}$	–	Design bending moment resistance, z-z axis
$M_{pl,Rd}$	–	Plastic moment resistance
$M_{el,Rd}$	–	Elastic moment resistance
$M_{N,Y,Rd}$	–	Reduced design bending moment resistance due to the presence of normal force, y-y axis
$M_{N,Z,Rd}$	–	Reduced design bending moment resistance due to the presence of normal force, z-z axis
M_{cr}	–	Critical moment for lateral torsional buckling
$N_{pl,Rd}$	–	Plastic normal resistance

N_{Ed}	–	Design normal force
n	–	Ratio of design normal force to design plastic resistance to normal forces
S_x	–	The section modulus
$V_{pl,Rd}$	–	Plastic shear force resistance
$V_{c,Rd}$	–	Shear force resistance
V_{ed}	–	Design shear force
$W_{el,min}$	–	Minimum elastic section modulus
W_{pl}	–	Plastic section modulus
Z_g	–	Distance between the shear center and the application point
α	–	Parameter introducing the effect of bi-axial bending
α_{LT}	–	Imperfection factor
β	–	Parameter introducing the effect of bi-axial bending
γ_{M0}	–	Partial factor
θ	–	Rotation
$\bar{\lambda}_{LT}$	–	Non-dimensional slenderness for lateral torsional buckling
ρ	–	Reduction factor for bending moment due to the shear force
Φ_{LT}	–	Value to determine the reduction factor χ_{LT}
χ_{LT}	–	Reduction factor for lateral torsional buckling

1 Introduction

1.1 Background

Beams with circular web perforation are known as cellular beams. These beams are popular in steel framed buildings with a span of 12m or longer, since they reduce the need for deep foundations and the cost of piled sites (Macsteel Service Centers SA, 2019).

Cellular beams have many advantages over other sections of steel beams. The web opening increases the depth-to-weight ratio of the beam, and therefore saves material. The increase in depth results in an increase of the section modulus (S_x) and the moment of inertia (I) of the beam. (Fares et al., 2016).

Figure 1 Service integration through the web-opening (Cellbeam Ltd, 2019)

Service integration, flexibility in the service distribution and ease of maintenance as shown in Figure 1, are some additional advantages which make the cellular beams an attractive alternative for the construction industry (New Steel Construction Magazine, 2019)

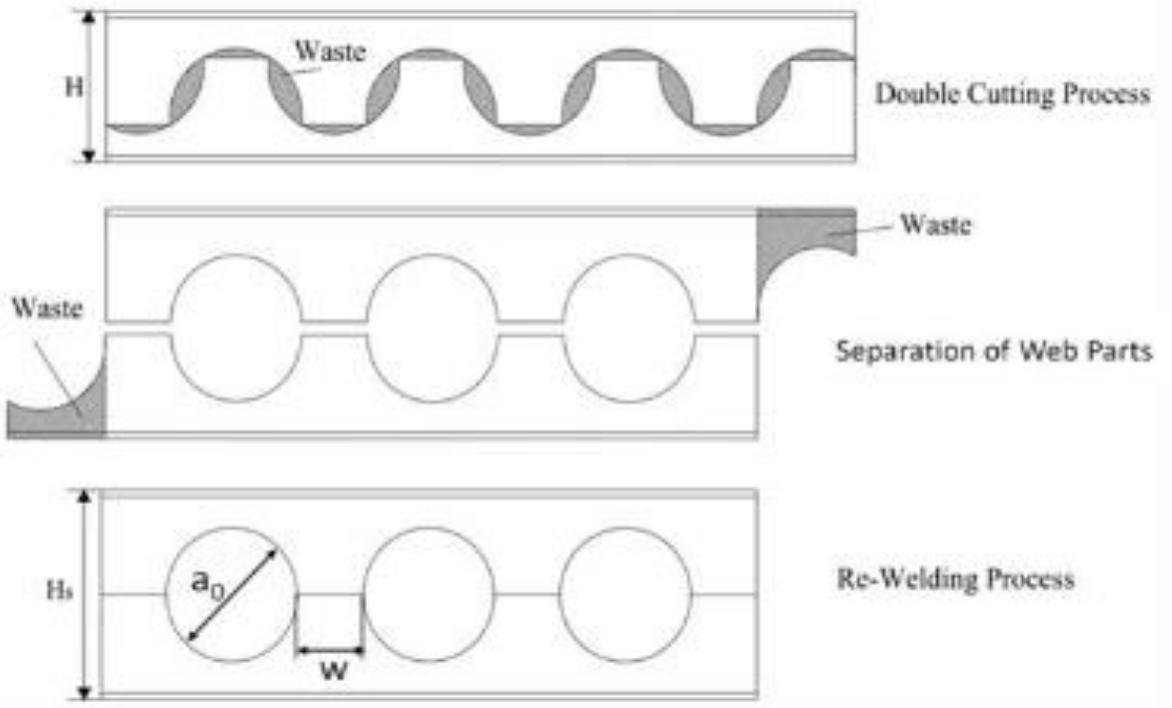

Figure 2 Fabrication process of the cellular beams

Chicago Bridge and iron works first introduced steel beams with web openings in 1910. In 1940s the use of perforated steel beams increased significantly. Cellular beams are produced by cutting a hot rolled steel beam along the centerline in a cellular pattern and then welding the two parts together as shown in Figure 2 (Fares et al., 2016).

The use of cellular beams in the construction industry in Norway is not widespread. There are few buildings in the country where cellular beams have been used. There is no production line of steel cellular members in Norway yet.

1.2 Area of focus

The area of focus of this thesis is to investigate the behavior of cellular beams. The topic of the thesis is to '*Investigate the behavior of cellular beams with different web-opening diameters through finite element (FEM) study'.*

In order to achieve the aim of the thesis, the following subtopics are thoroughly analyzed:

What is the effect of the diameter of the opening on the behavior of the beam?

How does the flange thickness affect the strength and the failure mode of the beam?

What is the effect of the web thickness on the behavior of the beam?

1.3 Limitations

The thesis is limited to the analysis of the behavior of cellular beams and further the following restrictions exist:

- The length of the beam analyzed is 1.7m
- The section of the beam is symmetrical
- The beam is a non-composite cellular beam
- Plastic analysis is not conducted

Cellular beams are approximately 40% to 60% deeper than their parent sections (Erdal et al., 2011). However, the modelled cellular beam has the same depth as its original section in order to maintain the same geometry as in the experimental analysis.

2 Theory

2.1 Buildings with cellular beams

Steel cellular beams have become popular in the construction industry due to their suitability to service integration and to the reduction of floor to floor height of a building. Cellular beams are preferred over the solid beams for long spans. In this chapter some examples of buildings where cellular beams have been used in the construction are presented.

Palestra office building in London (see Figure 3 below) is one of the major building projects in Europe where cellular beams have been used. This is a 12 storey office building, and cellular beams with a span 15m are utilized. Service ducts of 400mm diameter can pass through the web openings of the steel cellular beams, thus providing a significant advantage (Müller & Oppe, 2008).

Figure 3 Palestra House (Buildington database, 2011)

The internal view of Palestra house in the figure below shows pairs of continuous cellular beams that are connected on either side with the tabular columns made of circular hollow sections (CHS).

Figure 4 Inside of Palestra House (Lida Group, 2013)

IKEA commercial center in Nicosia-Cyprus, shown in Figure 5, is a business center of 22 000 m^2 and the steel frames costed 4 720 000 euros in the year 2007. The utilization of cellular beams contributes to more open floor plan and reduces the number of columns in the construction, therefore fewer foundation have been required. The heating, ventilation and air conditioning (HVAC) systems pass through the openings in the web (Constructalia, 2007).

Figure 5 IKEA commercial center (Constructalia, 2007)

The roof beams have been built with continuous cellular beams with spans of 16m to 24m. The cutting and welding process used in the fabrication of the cellular beams increase the total cost but the profit is in the weight reduction and in the material savings. The parent steel section HEA900 used in constructing the roof system of IKEA commercial center weighs 198 kg/m compared to the weight of the celluar beam which is 123.3 kg/m (Constructalia, 2007). The figure below shows the inside of the center.

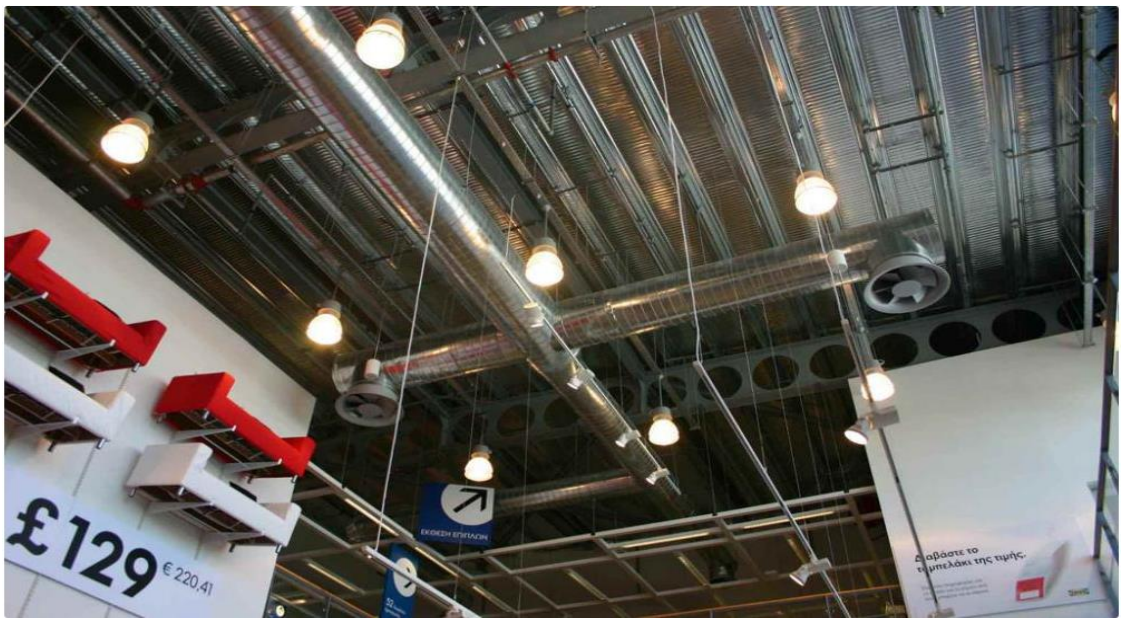

Figure 6 Internal view of IKEA commercial center (Constructalia, 2007)

The main conclusions that can be drawn from the usage of cellular beams in the two examples presented above are that the cellular beams are more suitable for spanning long distances and material savings and therefore provide an economically convenient alternative.

2.2 Steel

Steel is a popular material that people have been used for centuries for various purposes, whether it is construction of buildings, vehicles or machines. The composition and properties of the steel and its strength-to-weight ratio make steel favorable compared to other construction materials. In early civilization, iron ore is used to make primitive tools. It is believed that first iron furnace has appeared in about 1400 BC. Iron ore and charcoal were heated to high temperatures and iron makers removed impurities by hammering the metal. The industrial revolution made the demand for steel higher. Hot metal from blast furnace, steel scrap or mixture of both are the basic raw materials used in the production of steel. Steel can be defined as an iron with most of the carbon removed to make it tougher and ductile (British Constructional Steelwork Association, 2020).

According to the world steel association, 151.5 million tons of crude steel were produced in 2019 by 64 countries as illustrated in Figure 7, this corresponds to 2.8 % decrease compared to 2018. China is leading in production of crude steel worldwide with 81.5 million tones and Germany is the country in Europe with highest production with 3.3 million tones (Recycling Magazine, 2019).

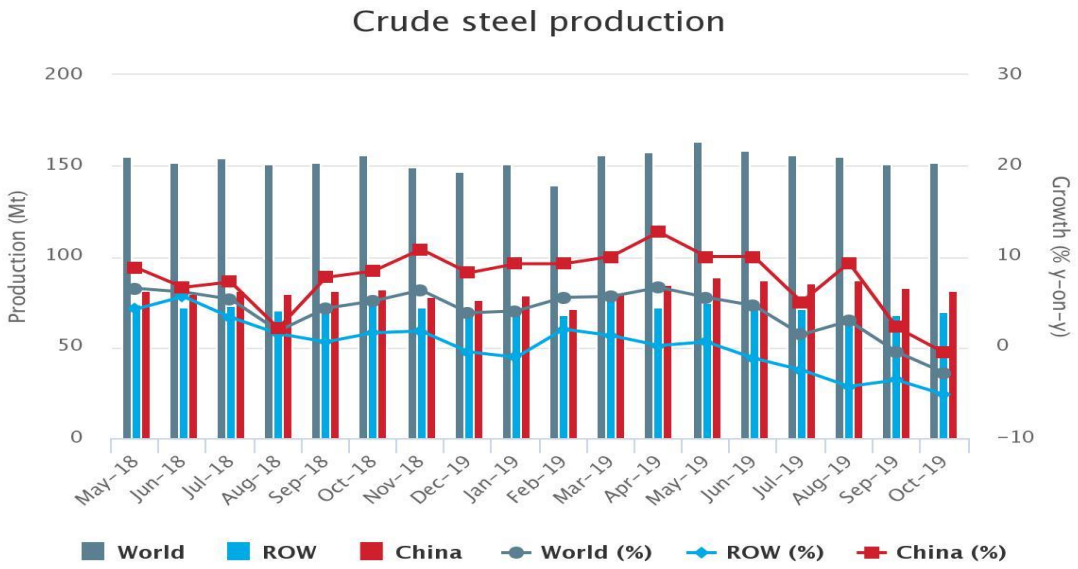

Figure 7 Crude steel production statistics

Structural steel grade S235 was popular in the construction industry for almost 30 year ago while today structural steel grade S355 is mainly used due to its chemical composition

to endure weathering and better mechanical properties. The trend to have stronger steel continues, and in some rare cases the use of steel with a yield strength from 700 to 1100 MPa is possible. The young modulus is independent on yield strength, the bending strength EI of a beam will not necessarily increase unless form of the section is modified. Apart from the strength of the steel, other factors are taken into consideration in high strength steel like displacement, stability and the dynamic quality (Larsen, 2010)

2.2.1 Types of steel products

Steel can be categorized into two types in terms of the process used in production:

1. Hot rolled steel

   The steel is roll-pressed at a very high temperature of about 1000 ^{o}C, which is over the recrystallization temperature of steel as shown in Figure 8. The steel is cooled after processing and this leads to shrinkage and there is less control over the final shape. Less processing is used in hot-rolled steel which makes it cheaper than the cold-rolled steel. In construction projects hot-rolled steel is commonly used (Reliance Foundry, 2020).

Figure 8 Hot rolled steel

2. Cold rolled steel

   Cold rolled steel is basically a hot rolled steel which is further processed under room temperature to achieve accurate dimensions and surface qualities, see Figure 9. This further processing comes with a higher price compared to the hot rolled steel (Reliance Foundry, 2020).

Figure 9 Cold rolled steel

2.2.2 Steel cross-section classifications

According to Eurocode, the classification of cross sections is based on the extent to which the local buckling resistance restricts the rotation capacity and resistance of the cross section (EC3-1-1, 2005). Steel beams are classified into four classes as shown in Figure 10. For a class 1 cross-section, the plastic moment (M_{pc}) capacity is attained with enough rotation (θ) capacity without reduction in the resistance. A class 2 cross-section is the one, which can attain plastic moment resistance with limited rotation resistance due to local buckling. A class 3 cross-section, elastic moment capacity (M_{ec}) is developed, however local buckling prevents the attainment of plastic moment resistance in the cross-section. A class 4 cross-section, local buckling occurs before the section reaches the elastic moment capacity (Chen et al., 2013).

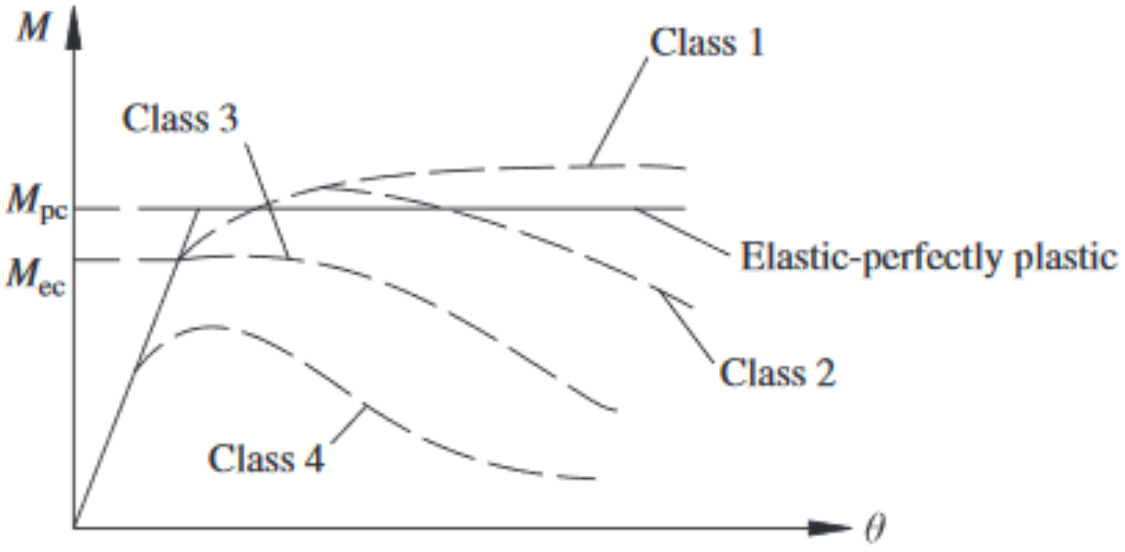

Figure 10 Cross section classification

2.2.3 Design of steel beams

A beam is defined as a member that resists shear force and bending.

In order to design a steel beam, the cross section must satisfy the requirements that are presented in Eurocode 3 (EC3-1-1, 2005).

1. **Uniaxial bending:** Clause 6.2.5 (1) in EC3-1-1

$$\frac{M_{Ed}}{M_{c,Rd}} \leq 1 \qquad (2.1)$$

Where M_{Ed} is the acting moment and $M_{c,Rd}$ is the moment capacity of the beam.

$$M_{c,Rd} = M_{pl,Rd} = \frac{W_{pl}\, f_y}{\gamma_{M0}} \quad \text{For class 1 and 2 cross sections} \qquad (2.2)$$

$$M_{c,Rd} = M_{el,Rd} = \frac{W_{el,min}\, f_y}{\gamma_{M0}} \quad \text{For class 3 cross sections} \qquad (2.3)$$

$$M_{c,Rd} = M_{el,Rd} = \frac{W_{el,min}\, f_y}{\gamma_{M0}} \quad \text{For class 3 cross sections} \qquad (2.4)$$

2. **Bi-axial bending:** Clause 6.2.9 (6) in EC3-1-1

$$\left[\frac{M_{y,Ed}}{M_{N,y,Rd}}\right]^{\alpha} + \left[\frac{M_{z,Ed}}{M_{N,z,Rd}}\right]^{\beta} \quad (2.5)$$

Where α =2; β= 5n but β≥1, n=$N_{Ed}/N_{pl,Rd}$ for I and H sections.

3. **Shear:** Clause 6.2.6 (1) in EC3-1-1

$$\frac{V_{Ed}}{V_{c,Rd}} \leq 1 \quad (2.6)$$

Where $V_{c,Rd}$ is either:

For the plastic shear resistance

$$V_{pl,Rd} = \frac{A_v(f_y/\sqrt{3})}{\gamma_{M0}} \quad (2.7)$$

where A_v is the shear area from clause 6.2.6 (3) of Eurocode 3.

Or

For elastic resistance

$$\frac{\tau_{Ed}}{f_y/(\sqrt{3}\gamma_{M0})} \leq 1 \quad (2.8)$$

4. **Bending and Shear interaction:** Clause 6.2.8 in EC3-1-1

The plastic moment resistance should be reduced if $V_{Ed} > 0.5\ V_{pl,Rd}$.

For I and H cross sections with equal flanges, bending moment about the major axis is calculated by:

$$M_{y,V.Rd} = \left(W_{pl,y} - \frac{\rho A_w^{\ 2}}{4 t_w}\right)\frac{f_y}{\gamma_{M0}} \leq M_{y,c,Rd} \quad (2.9)$$

Where $\rho = \left(2V_{Ed}/V_{pl.Rd} - 1\right)^2$ and $A_W = h_w t_w$

5. **Lateral-Torsional Buckling:**

The instability phenomenon which arises from the transversal displacement and rotation of a beam under bending moment is called lateral torsional buckling as illustrated in the figure below (Bresser et al., 2020).

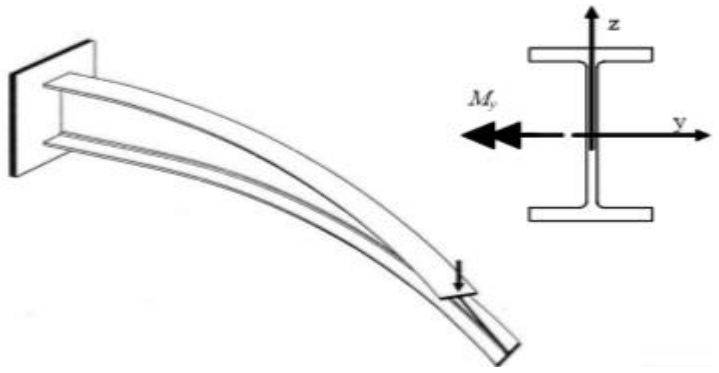

Figure 11 Lateral torsional buckling

The elastic critical moment M_{cr} is an important value when analyzing instability of beams, and it is defined as the maximum moment on a beam without any type of imperfections.

The elastic moment for a simply supported beam with double symmetric section is given by:

$$M_{cr} = C_1 \frac{\pi^2 EI_z}{(kL)^2} \left\{ \sqrt{\left(\frac{k}{k_w}\right)^2 \frac{I_w}{I_z} + \frac{(kL)^2 GI_t}{\pi^2 EI_z} + (C_2 z_g)^2} - C_2 z_g \right\} \quad (2.10)$$

Where

EI_z = the lateral bending stiffness

GI_T = torsional stiffness

I_w = warping stiffness

Z_g = Distance between the shear center and the application point

L = Distance between lateral braced section

k and k_w = Effective length factors

Lateral-Torsional Buckling resistance: Clause 6.3.2 in EC3-1-1

$$\frac{M_{Ed}}{M_{b,Rd}} \leq 1 \tag{2.11}$$

Where $$M_{b,Rd} = \frac{\chi_{LT} W_y f_y}{\gamma_{M1}} \tag{2.12}$$

χ_{LT} is a reduction factor which can be calculated as:

$$\chi_{LT} = \frac{1}{\Phi_{LT} + \left(\Phi_{LT}^2 - \bar{\lambda}_{LT}^2\right)^{0.5}} \tag{2.13}$$

but $\chi_{LT} \leq 1$

Where $$\Phi_{LT} = 0.5\left[1 + \alpha_{LT}\left(\bar{\lambda}_{LT} - 0.2\right) + \bar{\lambda}_{LT}^2\right], \tag{2.14}$$

α_{LT} is an imperfection factor

$$\bar{\lambda}_{LT}^2 = \sqrt{\frac{w_y f_y}{m_{cr}}} \tag{2.15}$$

Table 1 Imperfection factors for lateral torsional buckling curves

Buckling curve	A	b	c	d
Imperfection factor α_{LT}	0.21	0.34	0.49	0.76

Table 2 Values for lateral torsional buckling curves

Cross-section	Limits	Buckling curve
Rolled I-sections	h/b ≤ 2 h/b > 2	a b
Welded I-sections	h/b ≤ 2 h/b > 2	c d
Other cross-sections	-	d

2.3 Perforated steel beams and their usage

Castellated and cellular beams are the most popular types of perforated steel beams. These two types are used in various constructions, like parking facilities, industrial buildings, warehouses, schools, hospitals and office buildings. These types of beams are ideal for long span and open space solutions (Fares et al., 2016).

Figure 12 Parking facility

For parking facilities with longer span, the serviceability is more important than the strength. The web openings allow the light to go through, which brightens up inside the building as shown in Figure 12 (Fares et al., 2016). The combination of low height with more light inside the building, increases the comfort of the users since they feel that the building is more spacious in comparison with solid web beams building solutions.

Figure 13 Industrial facility

Mezzanines are used in industrial buildings to provide space for air handling equipment, process equipment and offices. The use of perforated steel beams help in reducing the need for more columns to support the mezzanine as shown in Figure 13 (Fares et al., 2016).

Figure 14 HVAC routing

Service utilities running through the web openings is one of the main advantages of buildings with perforated steel beams over the solid beams. The openings can be used for installation of HVAC, telephone wires and other equipment as shown in Figure 14 (Fares et al., 2016).

2.3.1 Advantages and disadvantages of cellular beams

Cellular beams were introduced in the steel construction industry in 1987, and since then 3500 projects in more than 20 countries have been built by using these beams. The steel construction institute in the UK has overseen full-scale destructive testing in various universities in the UK to verify their structural integrity and design criteria (Macsteel Service Centers SA, 2019). The use of cellular beams has increased in recent years and they are produced in a large scale as shown in the figure below (New Steel Construction Magazine, 2019)

Figure 15 Cellular beams

The advantages of cellular beams are the following:

- Service integration through the beam reduces the depth of the structure approximately 10-15 cm.
- Column free span as the cellular beams are ideal for long span of more than 12m.
- Higher load bearing capacity.
- Less foundation as there is no need for more columns.

The disadvantages of cellular beams are the following:

- Corrosion is a problem in exposed conditions thus frequent painting as a maintenance measure is recommended.
- Fireproof treatment is required.
- More complex analysis is necessary compared to solid sections.

2.3.2 Design procedures of the cellular beams

The steel cellular beams are susceptible to a higher number of failure modes in comparison to the solid beams (Fares et al., 2016).

The failure modes of the cellular beams can be divided into two categories: Global and local failures. The global failure mode is similar to that of the solid beam such as the bending, shear and lateral torsional buckling failure. The local failure modes which are unique for perforated steel beams are the Vierendeel mechanism and web-post buckling. The analytical method used to find the resistance of cellular beams is to compare the internal forces around the openings with the local resistance. The internal forces acting around the web opening are illustrated in Figure 16 (Sebastien et al., 2013).

2.3.3 The internal forces on the cellular beams

The internal forces are calculated from the global bending moment (M_{Ed}) and global shear force (V_{Ed}). The unknown normal ($N_{T,top}$) and shear forces ($V_{T,bot}$) acting on the top and bottom hinges are calculated using the following equations, (Sebastien et al., 2013):

$N_{T,top} = N_{T,bot} = M_{Ed}/d_G$, where d_G is the distance between $N_{T,top}$ & $N_{T,bot}$ (2.16)

$V_{T,top} = V_{T,bot} = V_{Ed}/2$ (2.17)

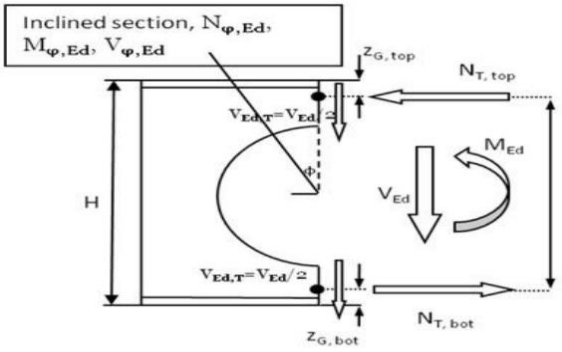

Figure 16 Internal forces around the web opening

2.3.4 Vierendeel mechanism

The shear force through the web opening creates a secondary moment, also called Vierendeel bending moment, at the tee sections of the cellular beam. The combination of the Vierendeel moment, the global bending moment and the shear force is called the Vierendeel mechanism (Panedpojaman et al., 2015). The figure below shows the formation of plastic hinges around the web opening due to the local bending of the top flange.

Figure 17 Vierendeel mechanism

Plastic hinges form at four points around the web opening where the shear force is highest, as shown in Figure 18. The global shear force through both top and bottom tee sections cause bending moment (Panedpojaman et al., 2015).

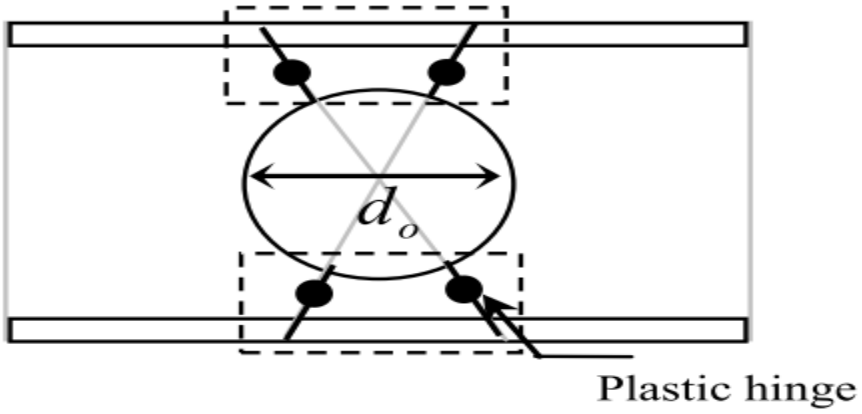

Figure 18 Plastic hinges

The internal forces at each inclined tee section by an angle φ as shown in Figure 16 is calculated by using the following equations (Sebastien et al., 2013):

$$N_{\varphi,Ed} = N_{T,top} * \cos(\varphi/2) + V_{T,top} * \sin(\varphi/2) \quad (2.18)$$

$$V_{\varphi,Ed} = N_{T,top} * \sin(\varphi/2) - V_{T,top} * \cos(\varphi/2) \quad (2.19)$$

$$M_{\varphi,top} = V_{T,top} * u - N_{T,top} * v \quad (2.20)$$

2.3.5 Web-Post buckling

The web-post buckling is created by the horizontal shear force acting through the web of the steel profile. The ultimate strength of the web-post is determined by either the flexural failure mode from the plastic hinges or the web-post buckling failure mode (Fares et al., 2016).

The internal forces acting on the beam induce a local bending moment. This bending moment generates a compressive stress which then leads to the web-post buckling mode as shown in Figure 19 (Sebastien et al., 2013).

Figure 19 Web-post buckling mode

Web-post buckling depends on the geometry and the material of the web-post. The intensity of the load acting on the tee sections is computed by using the following equations (Panedpojaman et al., 2014):

$$V_{t,U} = \frac{V * A_{st,U}}{A_{st,U} + A_{st,L}} \quad (2.21)$$

$$V_{t,L} = \frac{V * A_{st,U}}{A_{st,U} + A_{st,L}} \quad (2.22)$$

Where L stands for the lower part and U stands for the upper part of the tee sections. V is the vertical load acting through the centerline of the web opening, A_{st} is the shear area

of the tee sections which is calculated as: $A_{st} = s_t * t_w$. Here s_t denotes the height to depth ratio of the tee sections and t_w is the web thickness.

The applied vertical load causes compressive and tensile stresses across the web-post along its diagonal, known as strut action, and the horizontal shear force V_h acts in the middle of the web-post, as shown in Figure 20.

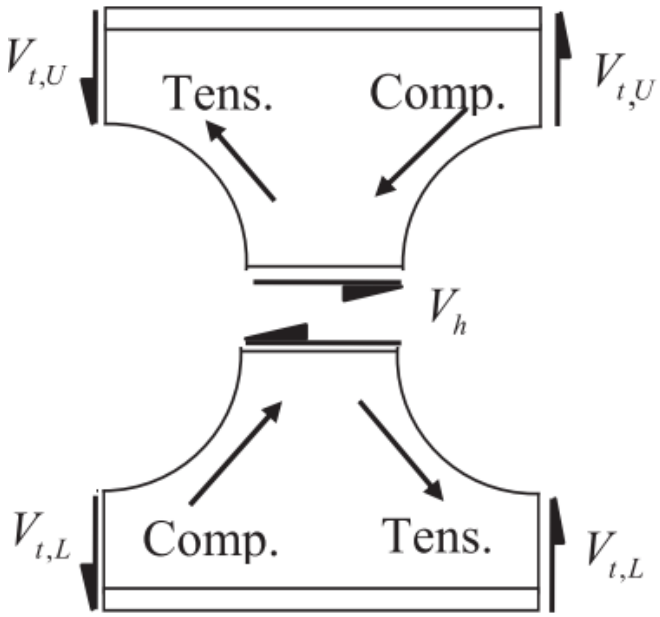

Figure 20 Forces acting on the web-post (Panedpojaman et al., 2014)

The compressive force on the diagonal (strut) is assumed to be equal to the applied load on the tee sections, thus the compressive stress (σ_c) of the strut is calculated as following:

$$\sigma_c = \frac{V_t}{b_e * t_w} \leq p_c \tag{2.23}$$

From the equation above, the buckling shear capacity can be computed as:

$$V_t = b_e * t_w * p_c \tag{2.24}$$

Where b_e denotes the effective width of the web-post, and p_c is the compressive buckling strength.

2.3.6 Von Mises stress

The turning point of elasticity theory in mechanics was the work of Robert Hooke in the 17th century. In the 19th century the quantitative and mathematical theory of elasticity got prominence; the continuum mechanics allowed the modelling of elastic phenomenon by using integral and differential calculus. The maximum distortion energy theory which applied to ductile materials has been derived from the continuum mechanics by Hubert in 1904. This theory was further developed by Von Mises in 1913 and got the name Von Mises stress (Simscale, 2020).

Figure 21 adopted from (Simscale, 2020) illustrates the stress-strain response from a simple tension test of a mild steel beam. The highlighted points in the figure are defined as the following:

Elastic limit: The deformation is reversible under this point since the energy is not lost.
Upper yield point: This is the critical point at which the deformation becomes permanent.
Lower yield point: This is the limit at which the strain increases at constant stress.
Rupture point: This is the point at which the steel fractures.

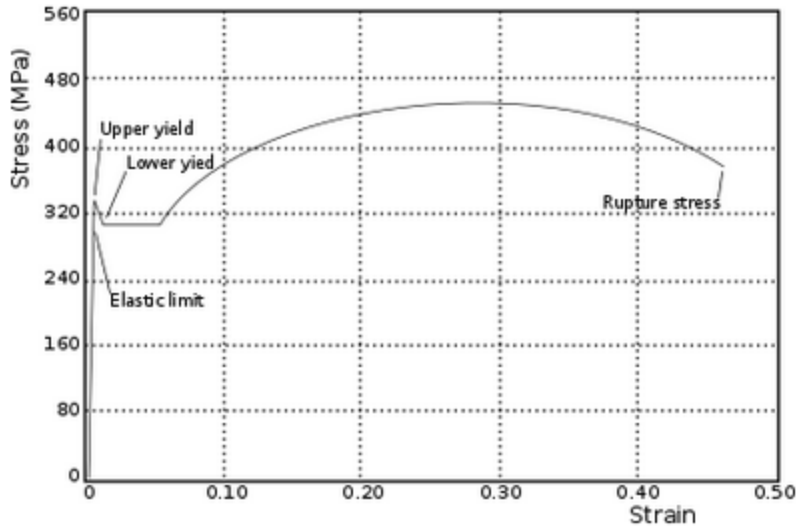

Figure 21 Stress strain curve

Von Mises stress indicates the yielding point of the material and it is used for ductile materials. The Von Mises yield criterion describes how the material yields if the stress in the material under load is equal to or greater than the yield capacity of the material (Simscale, 2020).

2.4 Finite element method (FEM)

The behavior of structure under given loading conditions is challenging task for engineers. Finite element method decomposes a complex structure into an equivalent network of simpler elements, and the resultant pattern of the all elements is called finite element mesh. The accuracy of the solution depends on the number of the meshes used, the more elements in the mesh the more accurate result is achieved. When the number of elements is increased, the calculation time also increases. The boundaries of elements are defined by points known as nodes. Each node is able to move both horizontally or vertically (Nikishkov, 2004).

The force (s) acting on the node is calculated by multiplying the stiffness of the element (k) by its displacement (r).

$$s = k * r \tag{2.25}$$

We carry out this process for every element in the mesh so that we set up the stiffness matrix for each element, the important step is to combine all these individual matrices into a single large matrix representing the stiffness of the whole system. The global matrix for the whole element is represented by:

$$F = K * V \tag{2.26}$$

Where

F is the global force

K is the stiffness matrix of the global system

V is the displacement vector of the global system

Before final global solutions are carried out, the boundary conditions, which were not taken into consideration in the element matrix, should be applied (Nikishkov, 2004).

2.4.1 The Finite element analysis procedure

When a structure or a structural element is loaded, they tend to deform thus causing challenging physical problems that engineers examine. An efficient and popular method that engineers use to convert the physical problem into mathematical model is the finite element method (FEM). Assumptions made in this procedure result in differential equations on which the mathematical model is based. The procedure is as presented in Figure 22 (Klaus-Jürgen Bathe, 2014).

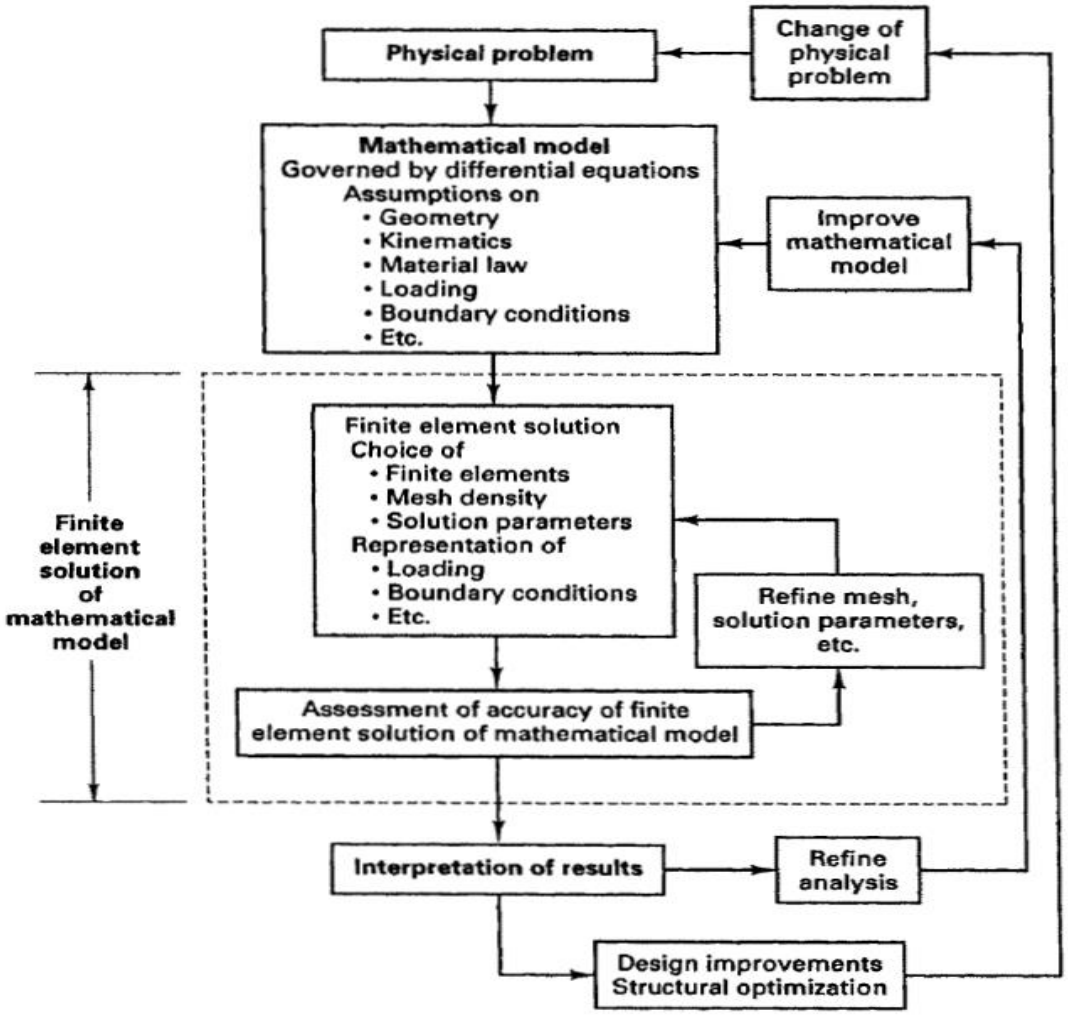

Figure 22 Finite Element Method overview chart

2.4.2 Displacement method

The Displacement method is one of the methods used in FEA solutions. The following steps must be followed in order to carry out the displacement method (Klaus-Jürgen Bathe, 2014):

- Idealize the whole structure into smaller elements joined by nodes.
- Identify local unknown displacements that define whole structural response.
- Calculate the unknown displacements from the force equilibrium equation.
- Find the local element stress distribution from the known displacements.
- Interpret the results from the analyses.

2.4.3 Mesh generation and refinement

When FEM is used, large structures are divided into smaller and simpler elements called finite elements. The purpose of meshing is to solve partial differential equations for the structure, each finite element in the mesh has a unique solution and their combination represent the solution for the complete mesh.

The following methods are used to generate meshes for the finite element analyses (Kittur & Huston, 1989):

- Mapped mesh

  This type of meshing is used for simple geometry. The user can define the number of elements in the system and FEM software generates the mesh by joining the nodes. This method is not commonly used.
- Free mesh

  This method is best suited to generating mesh for complex geometry. The structure is divided into sub-areas/sub-volumes and the number of elements is selected. Then the FEM program generates mesh that is suitable for the whole structure.

Mesh refinement

Meshes can be refined using one of the following three options (Kittur & Huston, 1989):

- H-method: the polynomial order of the shape function is kept constant while the number of elements is increased.

- P-method: The number of elements is kept constant while the polynomial order of the interpolation function is increased.
- R-method: The number of elements and the polynomial order of the shape function are kept constant while the nodes are redistributed.

2.5 Finite element software

The finite element package that has been used in the computational analysis is ANSYS Workbench. The Workbench has been used together with ANSYS mechanical. The analysis is three dimensional and the geometry is drawn in DesignModeler.

Elastic analysis has been carried out and the load is applied as concentrated load at the midspan like the experimental test. The elements used in the FEM modeling are SHELL181. This element has four nodes and six degrees of freedom at each node. This element is most suitable for linear applications, Figure 23 illustrates the element configuration (ANSYS Workbench, 2019).

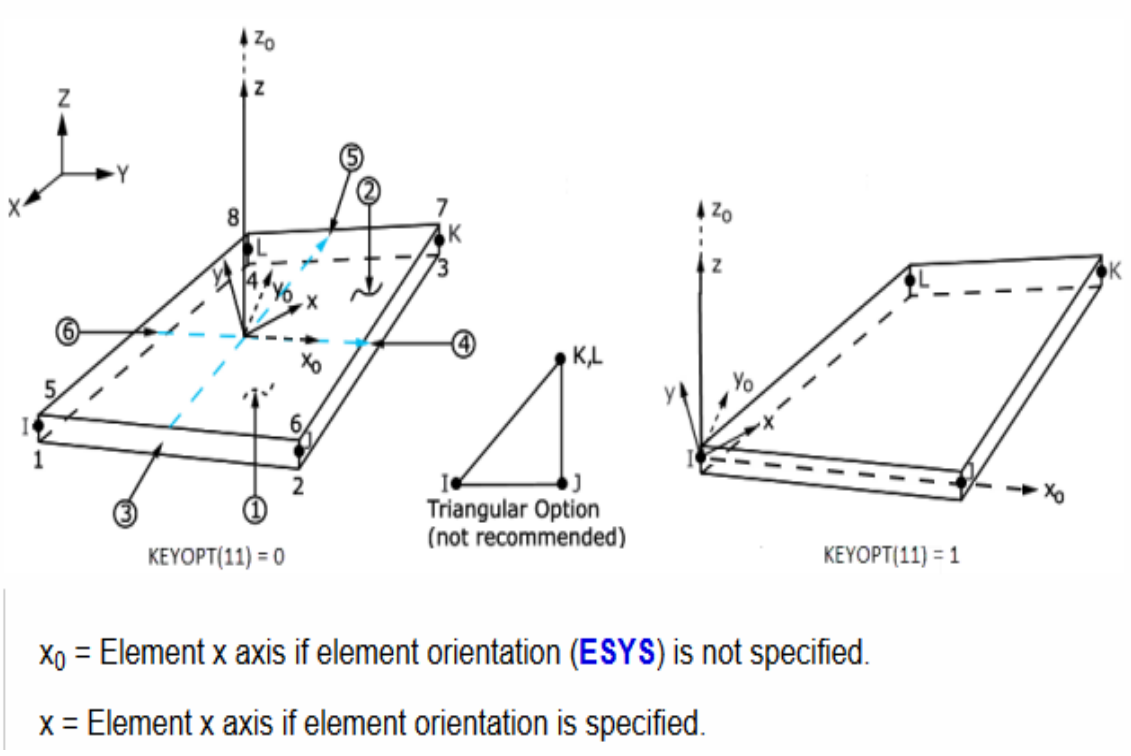

Figure 23 SHELL181 Element

2.5.1 Contact problems and analyses

Contact problems are categorized into two types:

- Flexible to flexible
- Rigid to flexible

Flexible to flexible contact problems are standard contact problems where all the bodies in contact have the same stiffness, an example of such a problem is a bolted connection between steel flanges. On the other hand a contact problem is defined as rigid to flexible contact problem when the contacting surfaces have significant different stiffness (ANSYS Inc., 2017).

Contact analyses

Contact problems are classified into the following three groups based on their properties (ANSYS Inc., 2017):

- General contact
- Pair-based contact
- Node to node contact

General and pair-based contact problems utilize surfaces for their contact definition, these types of contacts are used for small sliding and large sliding contact solutions.
When the position of the contact is known in advance, the node to node contact element is suitable for application. These types of contacts are used for solving small relative sliding contact surfaces. The following specifications should be defined for pair-based or general contacts (ANSYS Inc., 2017):

- ✓ The bodies that are in contact
- ✓ The pairing and interaction of the surfaces that are in contact with each other
- ✓ Friction coefficients of the behavior of the contacts
- ✓ Properties and parameters of the contacts
- ✓ Settings and formulations of the contacts

2.5.2 The capabilities of contact elements

Based on their capabilities, contacts are divided into five models, namely line to line, line to surface, surface to surface, node to surface and node to node. Each model is suitable for a particular contact problem and use a specific contact element (ANSYS Inc., 2017).

Node to surface contact elements

This type of contact elements supports large sliding, large deformation and different mesh configurations of contacting bodies. A typical node to surface contact element is CONTA175 which is used for flexible to flexible contacts or rigid to flexible contacts between nodes and surfaces. The target elements of this type of contact is TARGE169 or TARGE170 (ANSYS Inc., 2017).

Surface to surface contact elements

These contact elements are used for modeling flexible to flexible or rigid to flexible contact between surfaces. The contact elements and target element in surface to surface contact problems make contact pair: TARGE170 with CONTA173, CONTA174, CONTA175, CONTA176, or CONTA177 for 2D contact pair. TARGE169 with CONTA171, CONTA172, CONTA175 for 3D contact pair as shown below in Figure 24 (ANSYS Workbench, 2019).

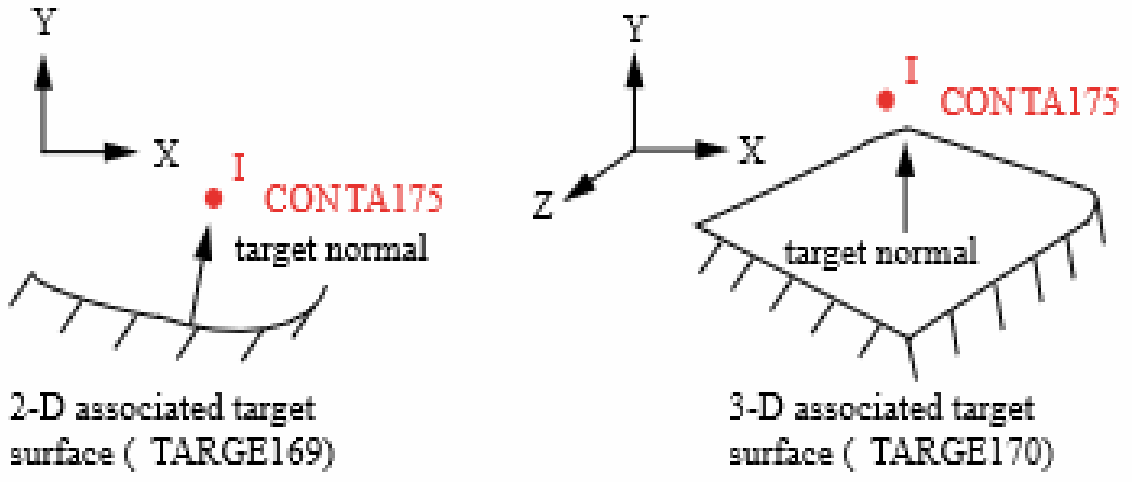

Figure 24 CONTA175 Element

Target element TARGE170 represents 3D target surfaces for contact element CONTA174 or CONTA175 which overlay the boundary of the solid or shell elements. CONTA175 and TARGE170 have been used by ANSYS for the analysis in this thesis. The target surface is modelled by using a set of target segments, as shown in Figure 25.

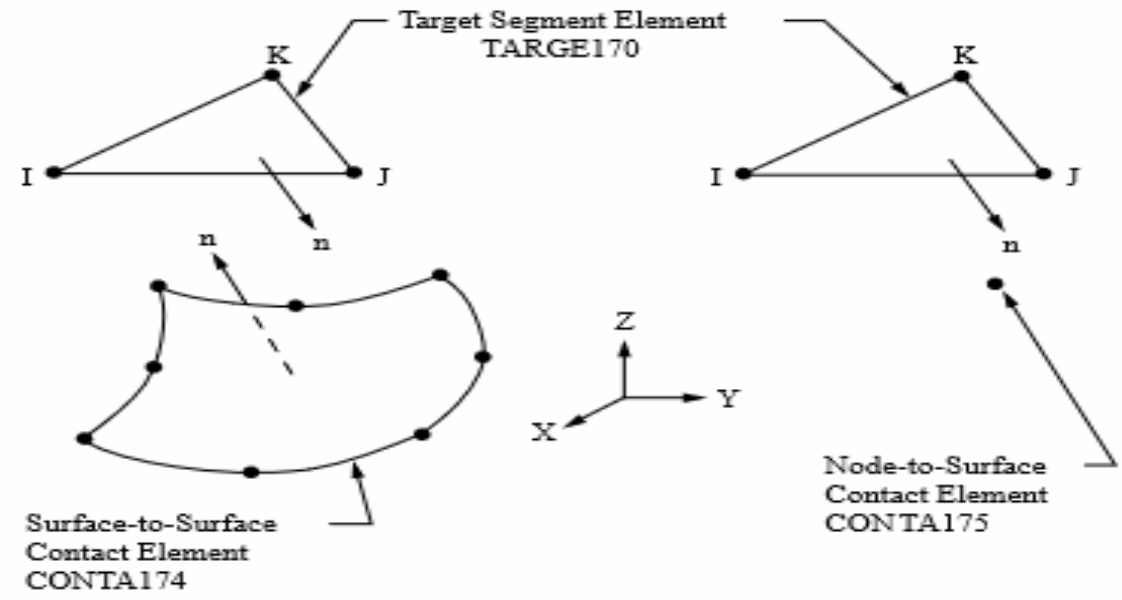

Figure 25 TARGE170 Element

3 Methodology

3.1 Modelling

The finite element model is based on universal beam UB457x152x52 of steel grade S355 with web opening diameter of 315mm. The diameter of the web opening, the thickness of the flanges and the web have been varied to investigate their effect on the capacity of the web-post. ANSYS software has been used to perform the elastic analysis. The simply supported beam is loaded at the midspan. The elastic modulus of the steel used in the model is 200 GPa and the Poisson ratio is 0.3.

The dimensions of the basis model as adopted from the experimental tests as shown in Figure 26 (Tsavdaridis & D'Mello, 2011). The center to center spacing (S) of the web openings is 1.3*d_0, where d_0 is the size of the diameter. The height of the modelled beam is 449,8mm. This is a short beam with a length of 1.7m.

Stiffeners have been placed at the supports and at the midspan. The stiffeners at the supports have thickness of 10.9mm similar the flange thickness, whereby the thickness of the stiffener at the midspan is 20mm.

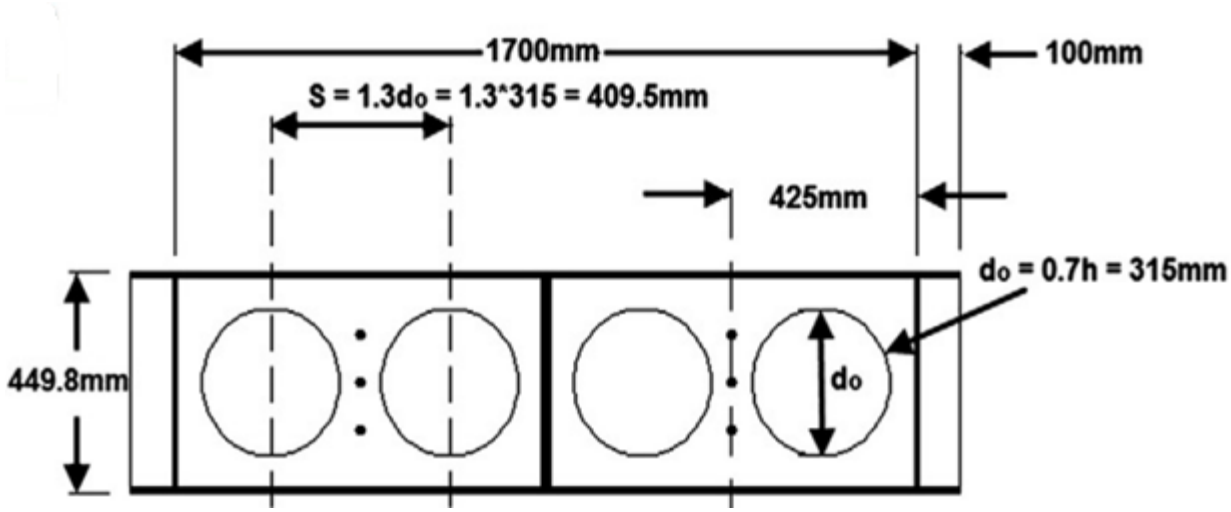

Figure 26 Dimensions of the cellular beam in the experiment

3.1.1 Finite element model

The dimensions, boundary conditions and the loading conditions of the finite element model analyzed are according to the experiment conducted by Tsavdaridis and Cedric D'Mello as shown in the figure below.

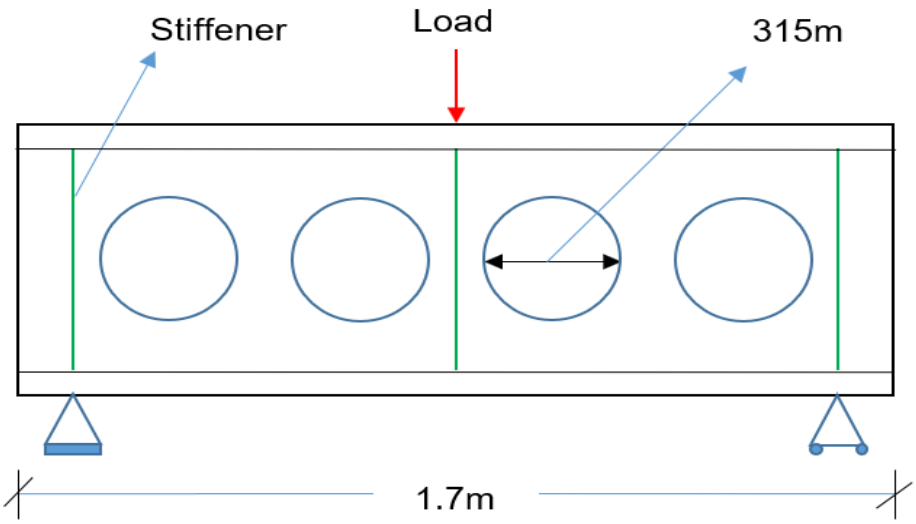

Figure 27 FEM model

3.2 Case studies

A parametric study on 12 cases has been carried out, using FEM analysis software, to investigate the effect of the different parameters on the beam. Each of the three main cases has four subcases.

Case 1a is the basis case from the experiment, where the diameter of the opening is 315mm, the thickness of the flanges is 10.9mm and the thickness of the web is 7.6mm. In case 1b changes are made to the web diameter from 315mm to 157.5mm and other parameters are kept the same. The diameter is reduced to 105mm in case 1c and in case 1d the beam is without perforations.

In case 2a the thickness of the flanges has been increased from 10.9mm to 19.6mm with web opening of 315mm while the web thickness is kept at 7.6mm. The results from this case analysis are compared to case 1a. The diameter of the opening of the web-post is

changed from 315mm to 157.5mm in case 2b and 105mm in case 2c. The results are compared to cases 1b and 1c respectively.

The thickness of the web is increased from 7.6mm to 11.4mm in case 3a with a diameter of 315mm while the thickness of the flanges is kept at 10.9mm. The result has been compared to case 1a. The diameter of the opening of the web-post has been changed from 315mm to 157.5mm in case 3b and 105mm in case 3c. The results have been compared to cases 1b and 1c respectively.

Subcases with indication d (1d, 2d and 3d) represent the strength of the beam without perforations. The results from these analyses have not been compared with the ones from the perforated beam since the failure modes are different thus leading in wrong conclusion.

The variations made on the parameters in the 12 cases are tabulated in table 3 below.

Table 3 Case studies

Case nr.	**Parameter variation**
1a	Basis case
1b	The opening diameter reduced from 315mm to 157.5mm
1c	The opening diameter reduced from 315mm to 105mm
1d	Web without perforation
2a	The flange thickness increased from 10.9mm to 19.6mm with opening diameter of 315mm
2b	The flange thickness increased from 10.9mm to 19.6mm with opening diameter of 157.5mm
2c	The flanges thickness increased from 10.9 mm to 19.6mm with opening diameter of 105mm
2d	The flanges thickness increased from 10.9 mm to 19.6mm without perforation
3a	The web thickness increased from 7.6 mm to 11.4mm with opening diameter of 315mm
3b	The web thickness increased from 7.6mm to 11.4mm with opening diameter of 157.5mm
3c	The web thickness increased from 7.6mm to 11.4mm with opening diameter of 105mm
3d	The web thickness increased from 7.6mm to 11.4mm without perforation

4 Results

The results from the different cases modelled in the FEM program, ANSYS Workbench will be presented in this chapter. The results are further discussed in chapter 5 and the conclusion are presented in chapter 6.

4.1 Case 1

Table 4 Results from case 1

Subcase	Diameter [mm]	Yield load [kN]	Max. Deflection [mm]	Failure mode
a	315	255	1.3	Web-post buckling
b	157.5	324.5	0.88	Web-post buckling
c	105	343	0.80	Web-post buckling
d	Without perforation	620	0.95	Top flange buckling

In subcases a, b, and c the failure mode is web-post buckling. In subcase d the weaker part in the beam is the flange and failure occurs at the top flange as presented in Table 4.

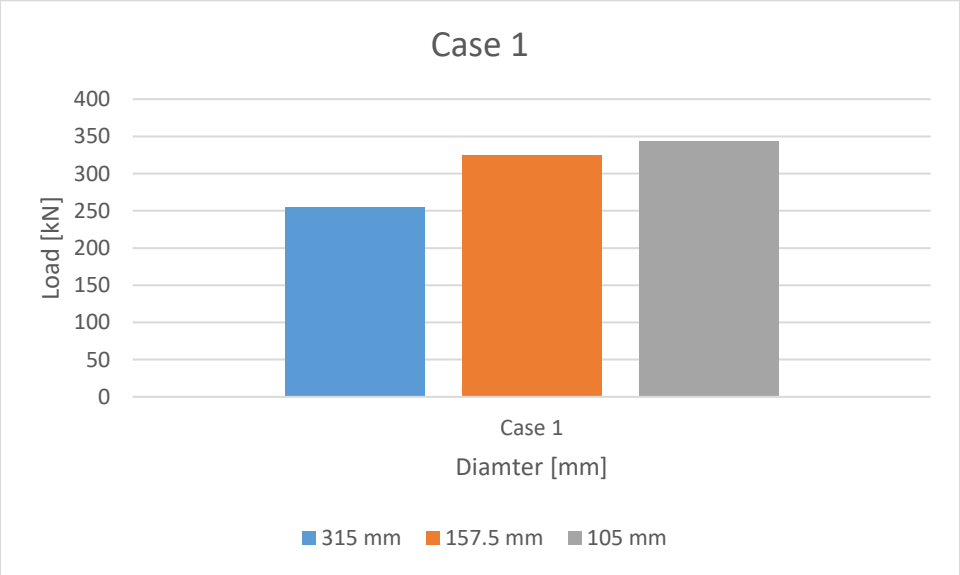

Figure 28 Load-diameter graph of cases 1

The web-post strength increases with the decrease in the diameter of the opening as illustrated in Figure 28.

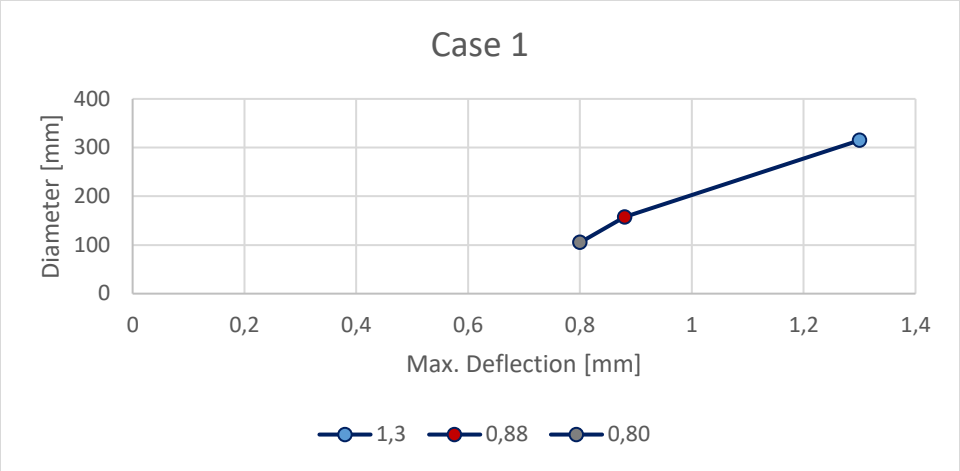

Figure 29 Diameter-deflection chart of cases 1

Though the deflection is not significant in this short beam, however there is a linear relation between the opening diameter and the deflection, whereby the deflection decreases with the decrease of the diameter. The deflection in subcase d is not included in the figure above, because the maximum deflection takes place at the top flange and therefore cannot be compared with the deflection data for the other subcases.

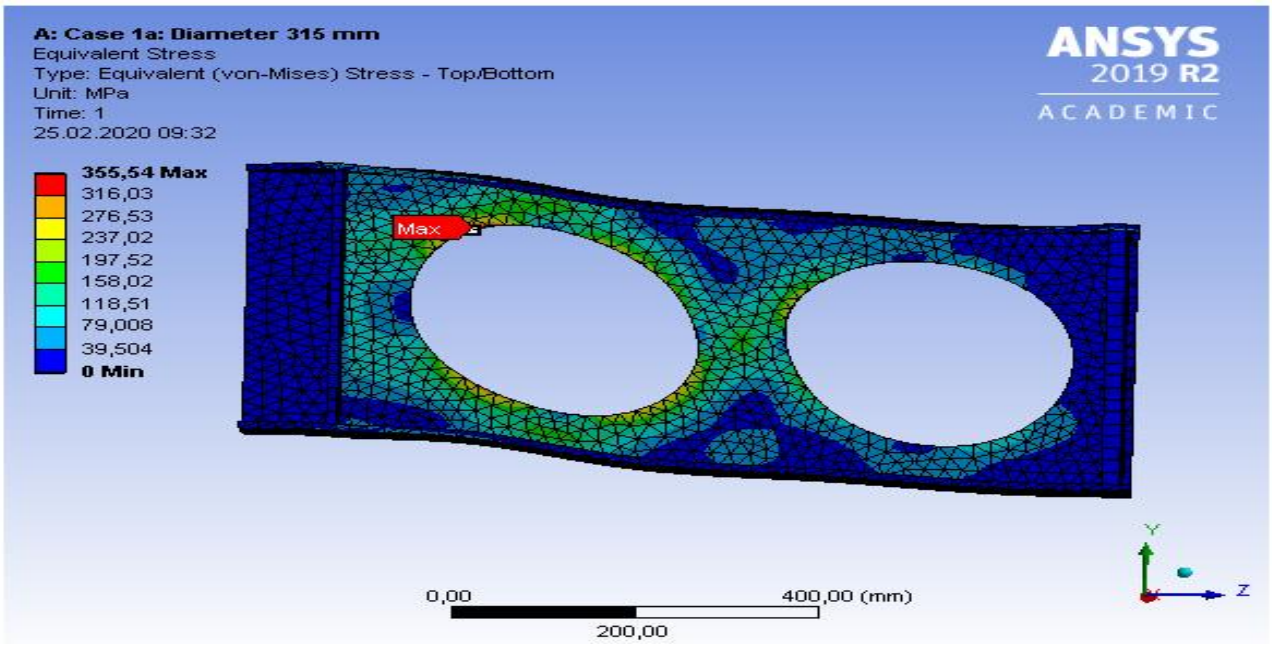

Figure 30 Von mises stress in case 1a

Maximum equivalent stress at which the failure occurs is concentrated around the web opening as shown in Figure 30.

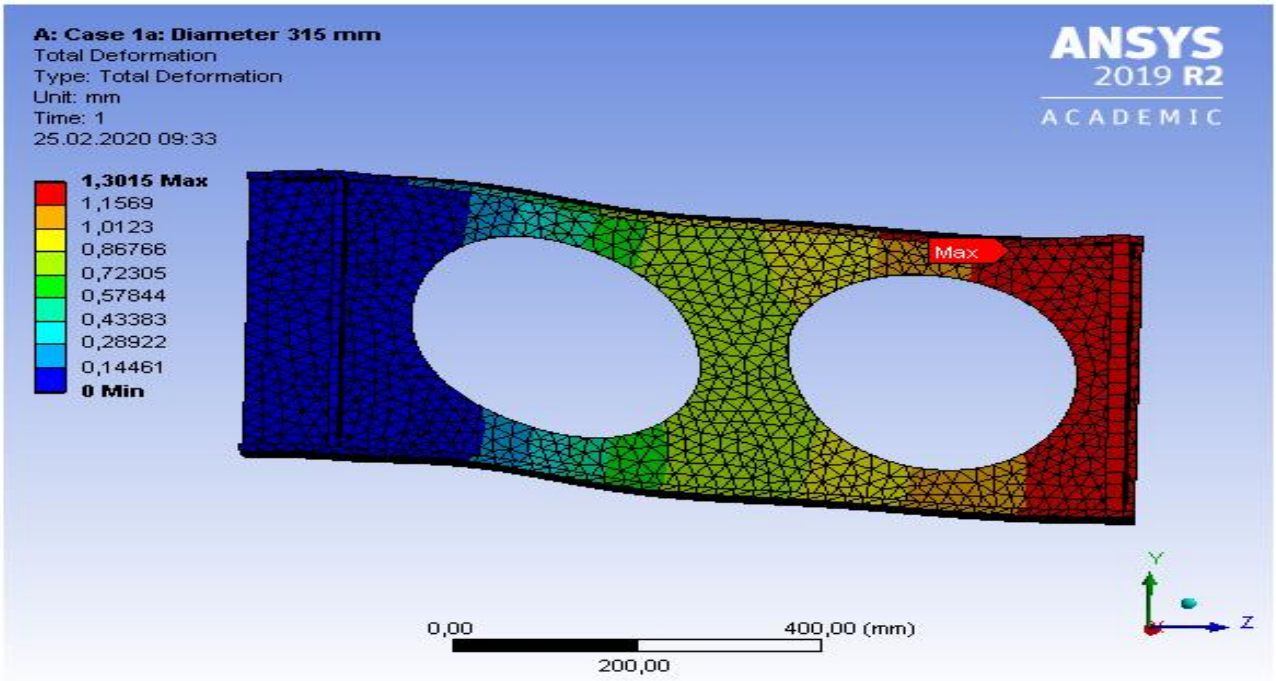

Figure 31 Deflection in case 1a

Figure 31 above shows deflection of 1.3mm at the mid-span in case 1a.

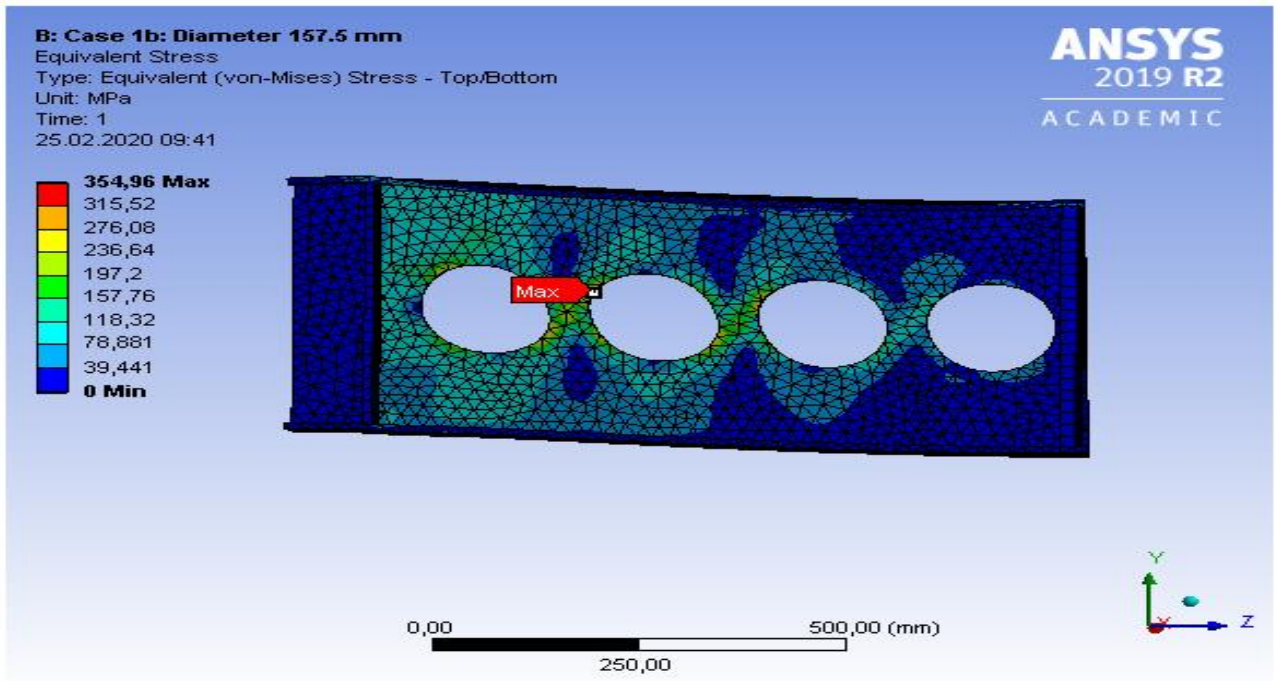

Figure 32 Von mises stress in case 1b

The maximum stress at which the web-post buckles is around the openings in subcase 1b as shown in Figure 32.

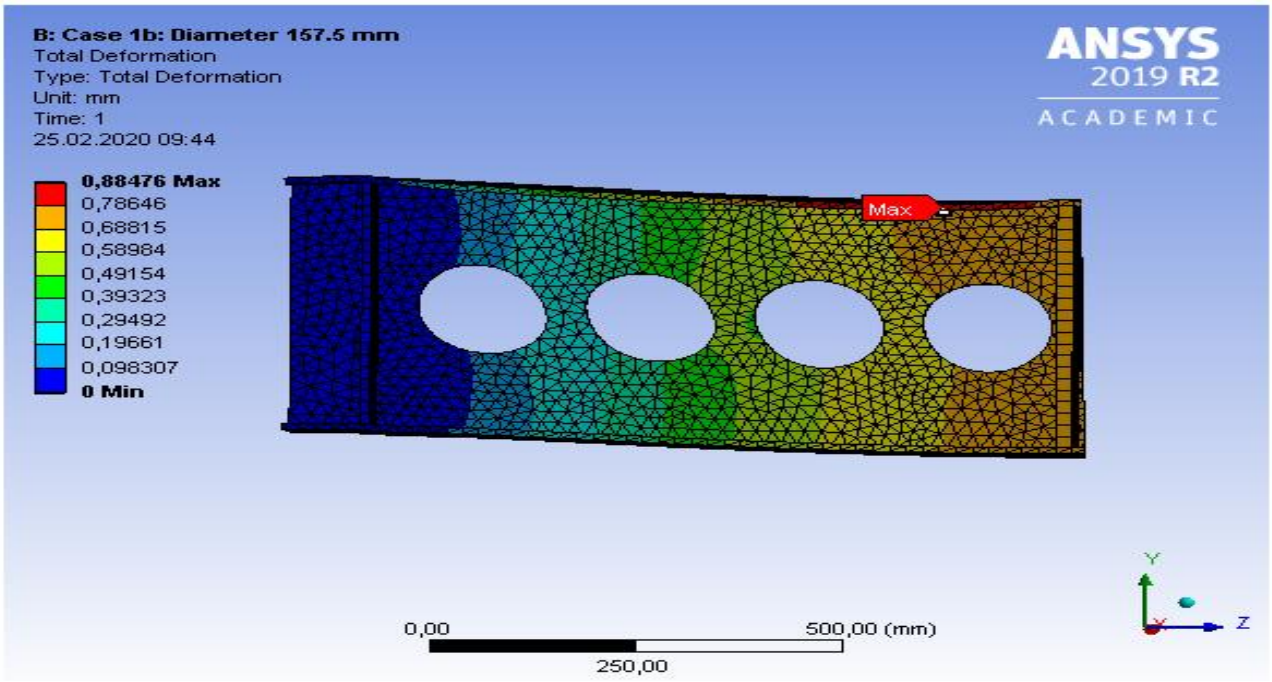

Figure 33 Deflection in case 1b

The deflection decreases as the diameter of the web opening decreases in subcase 1b. The maximum deflection is 0.88mm shown in Figure 33.

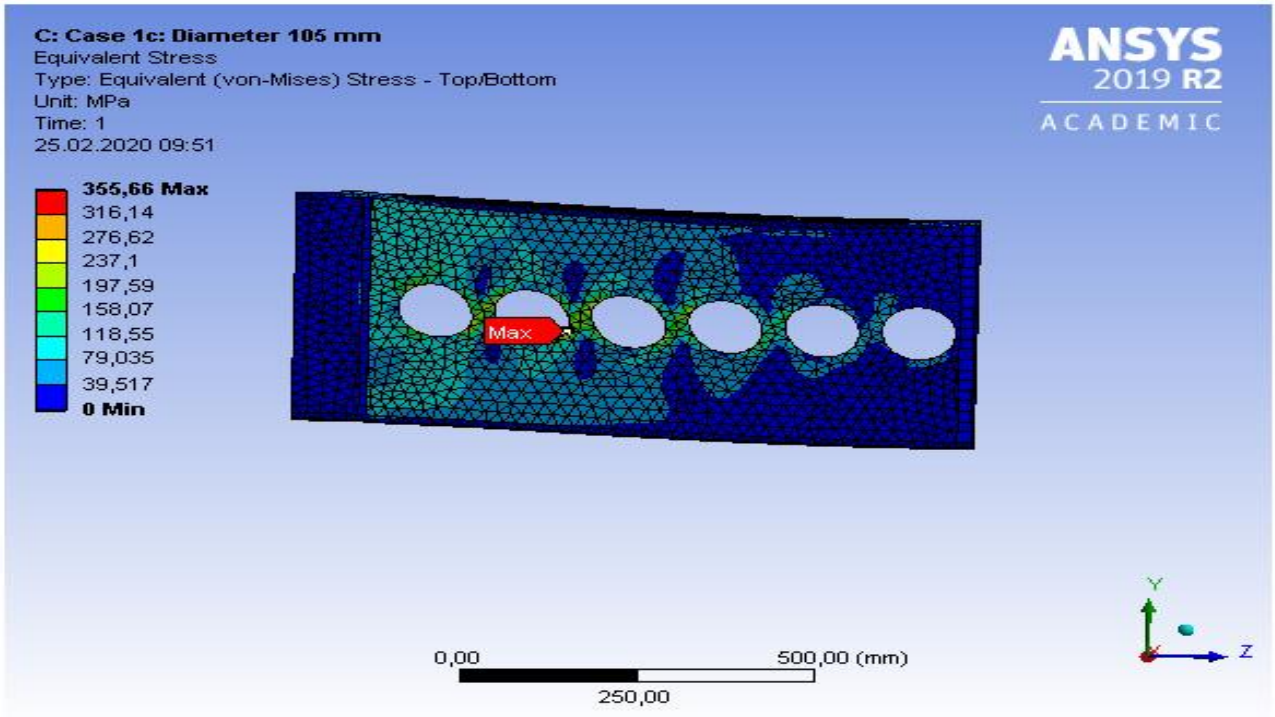

Figure 34 Von mises stress in case 1c

With reduced diameter of the web opening, the failure mode is web-post buckling and the highest stress is found in the vicinity of the web opening (see Figure 34).

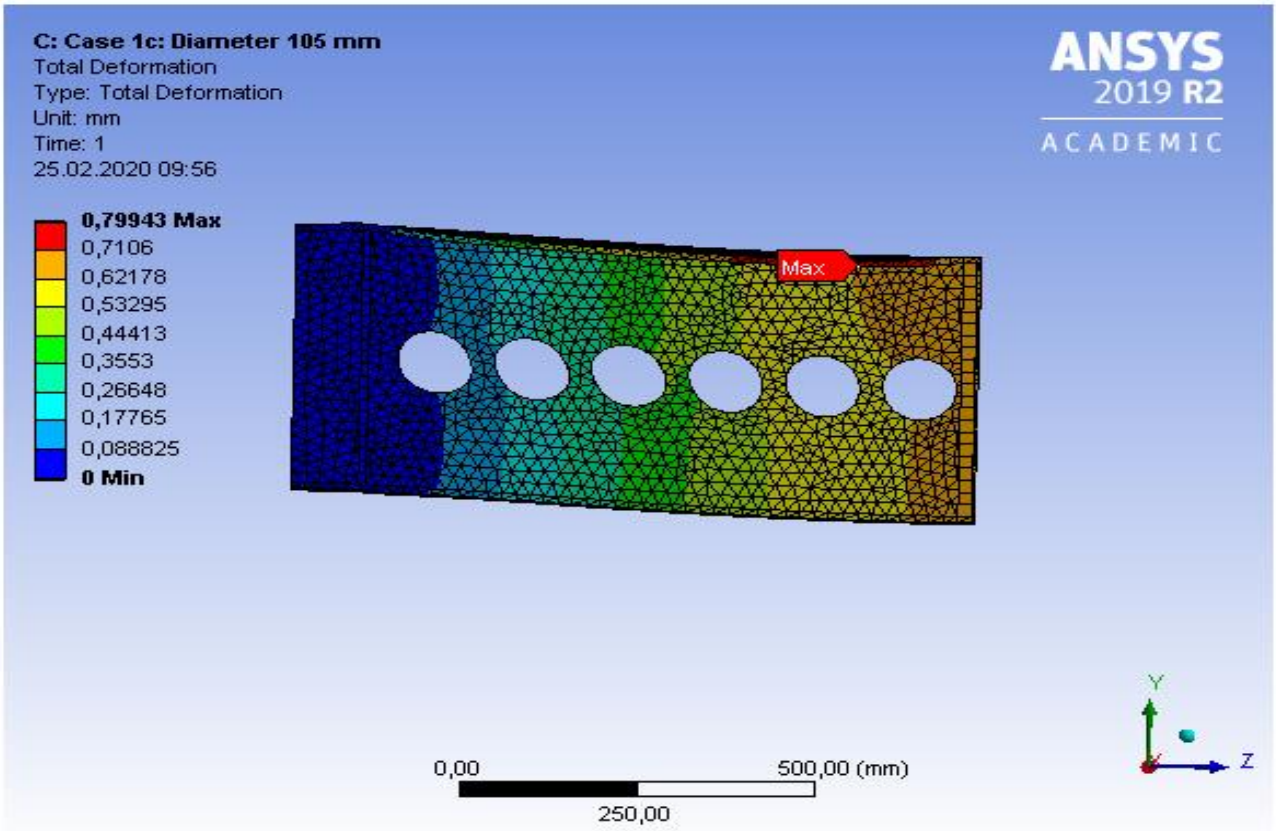

Figure 35 Deflection in case 1c

Figure 35 shows the deflection further decreases with the decrease of the web opening in subcase 1c.

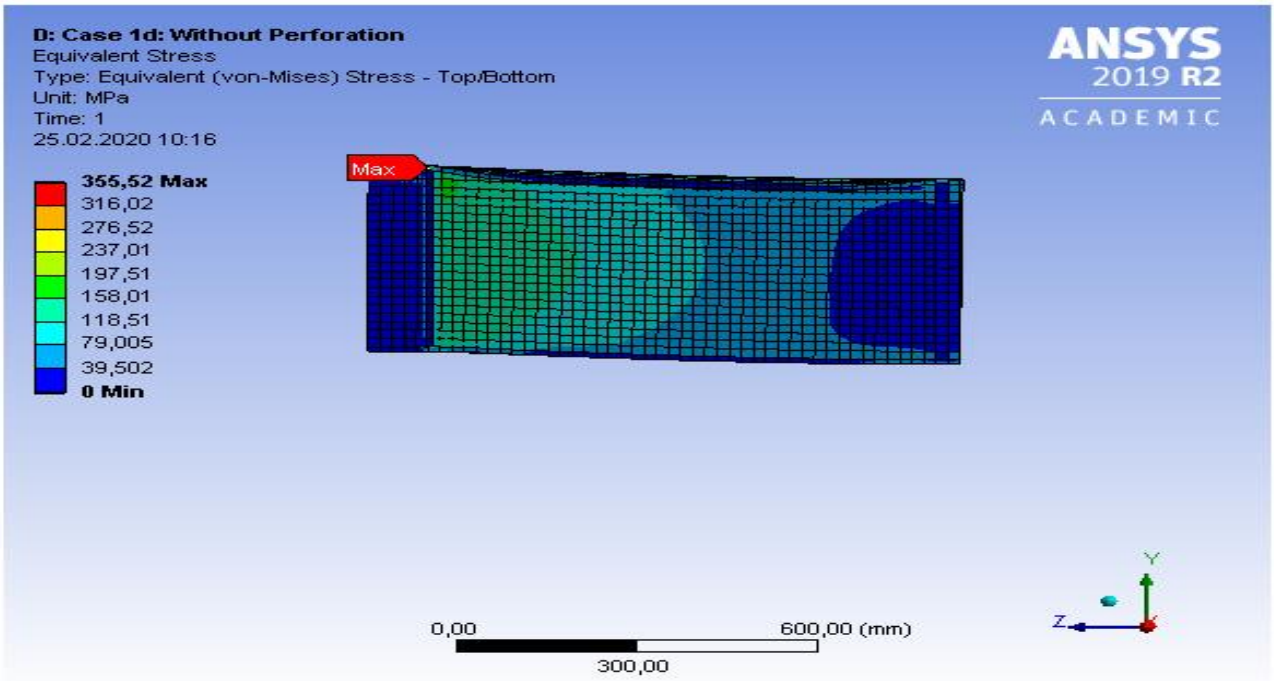

Figure 36 Von mises stress in case 1d

In subcase 1d the failure mode is the top flange buckling , since the weakest part is the flange itself as shown in Figure 36.

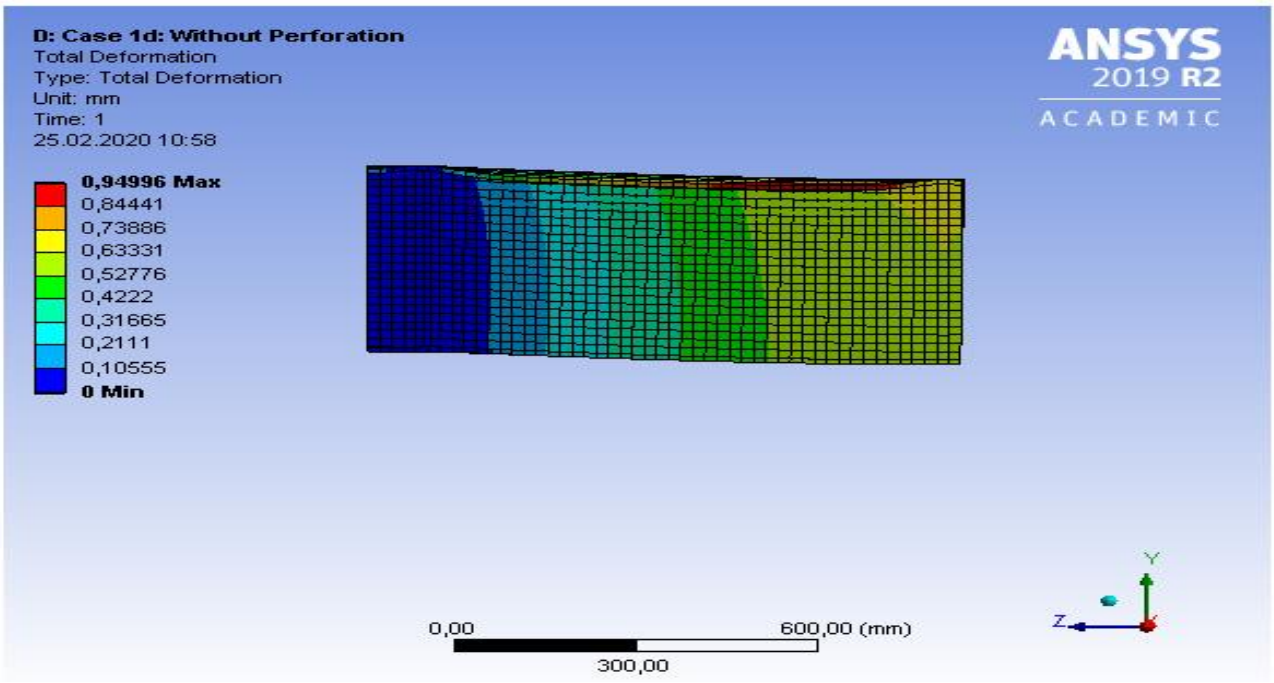

Figure 37 Deflection in case 1d

The maximum deflection in case 1d occurs at the top flange, as shown in Figure 37.

4.2 Case 2

Table 5 below shows the maximum load the beam can support, the failure mode and the maximum deflection thereof. The failure mode is web-post buckling for subcases a, b and c. The top flange buckling is the failure mode in subcase d.

Table 5 Results from case 2

Subcase	Diameter [mm]	Yield load [kN]	Max. Deflection [mm]	Failure mode
a	315	266	1.2	Web-post buckling
b	157.5	331	0.76	Web-post buckling
c	105	354	0.66	Web-post buckling
d	Without perforation	995	1	Top flange buckling

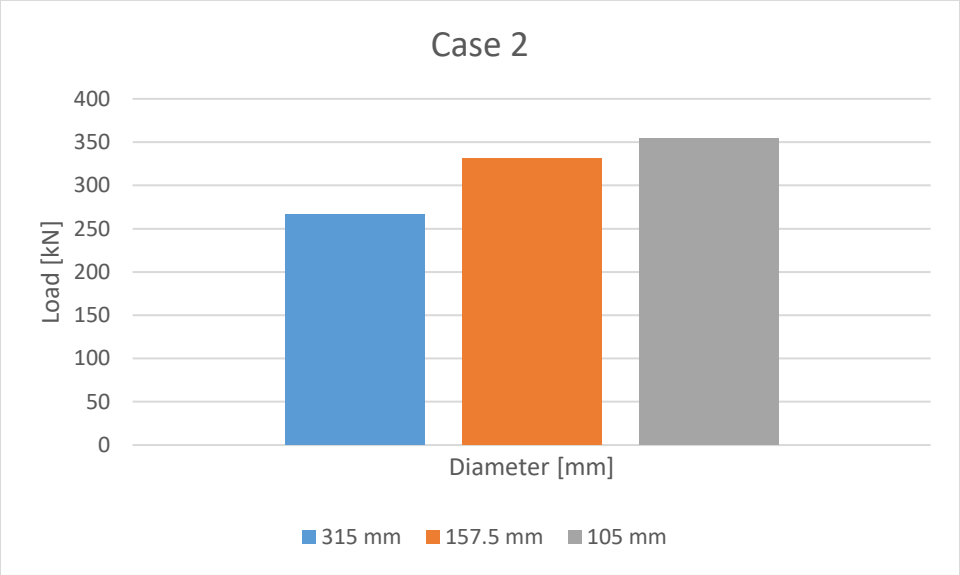

Figure 38 Load-diameter overview of case 2

The load bearing capacity of the beam increases with the decrease in diameter as illustrated in Figure 38.

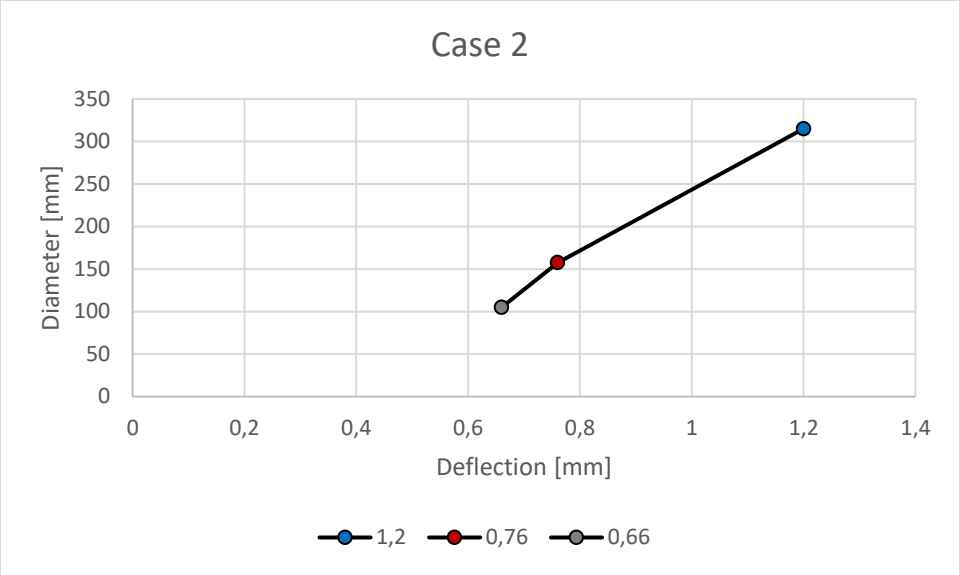

Figure 39 Diameter-deflection chart of case 2

The deflection decreases with the decreasing opening diameter as shown in the figure above.

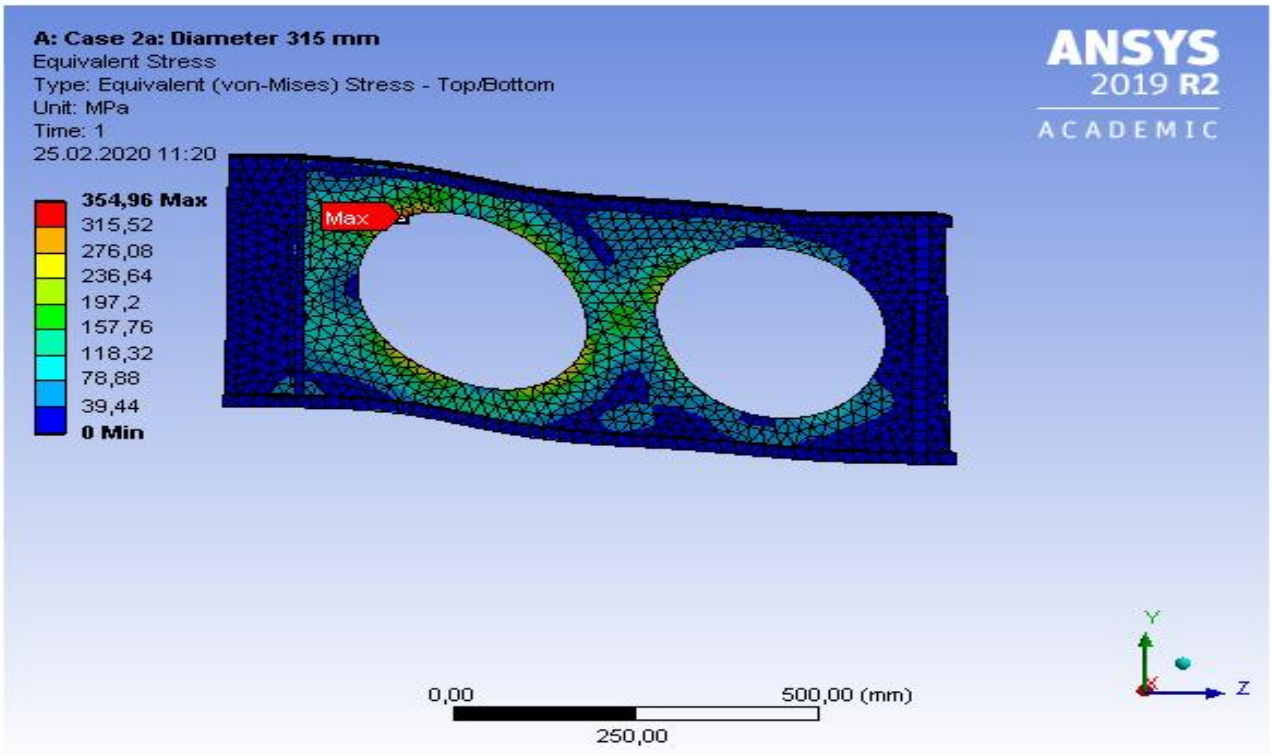

Figure 40 Von mises stress in case 2a

The web-post buckles and the maximum stress is around the opening as shown in Figure 40.

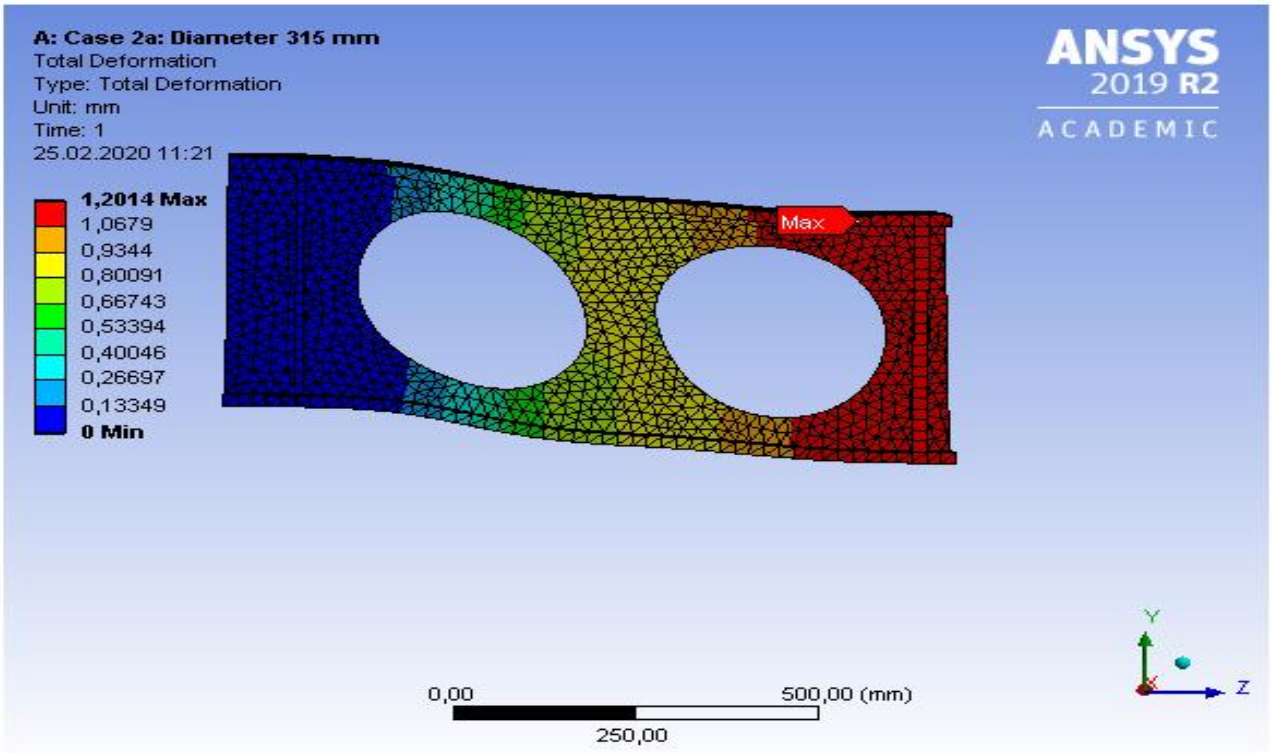

Figure 41 Deflection in case 2a

The maximum deflection is at the mid-span and its magnitude is 1.2mm, see Figure 41.

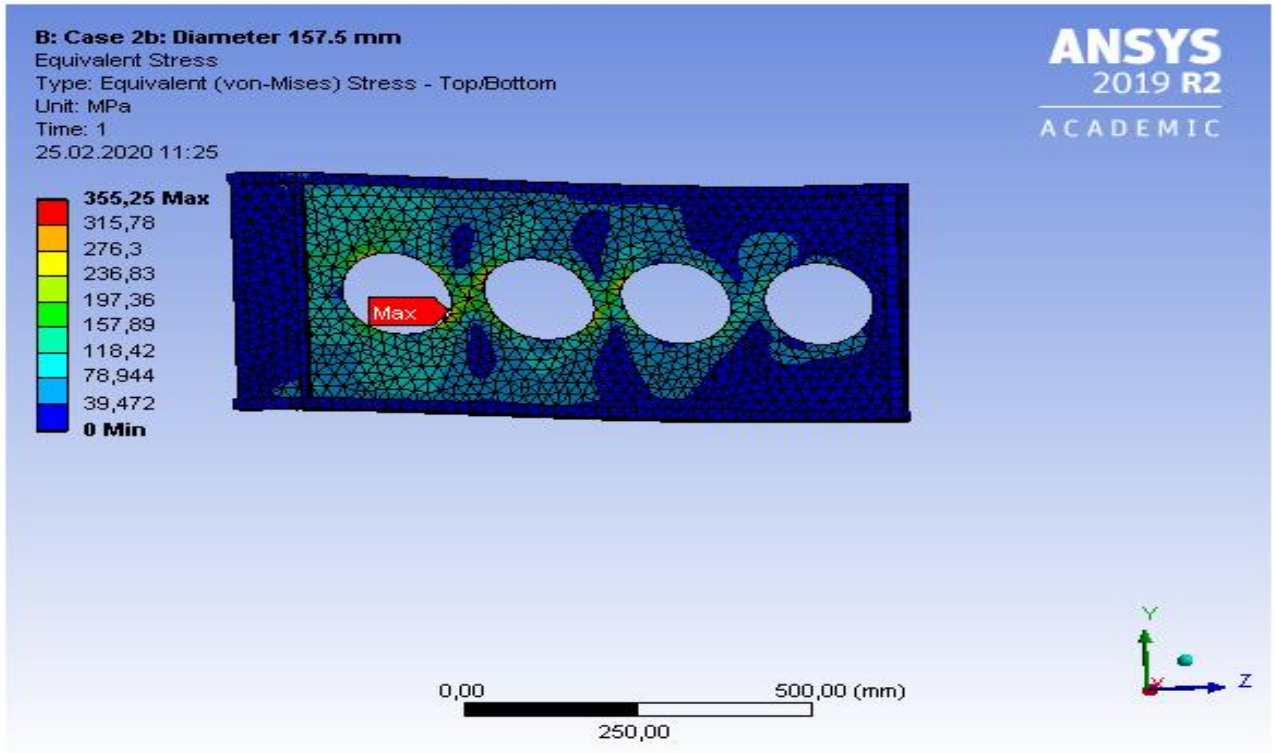

Figure 42 Von mises stress in case 2b

The failure mode is web-post buckling and the maximum stress around the opening as show in Figure 42.

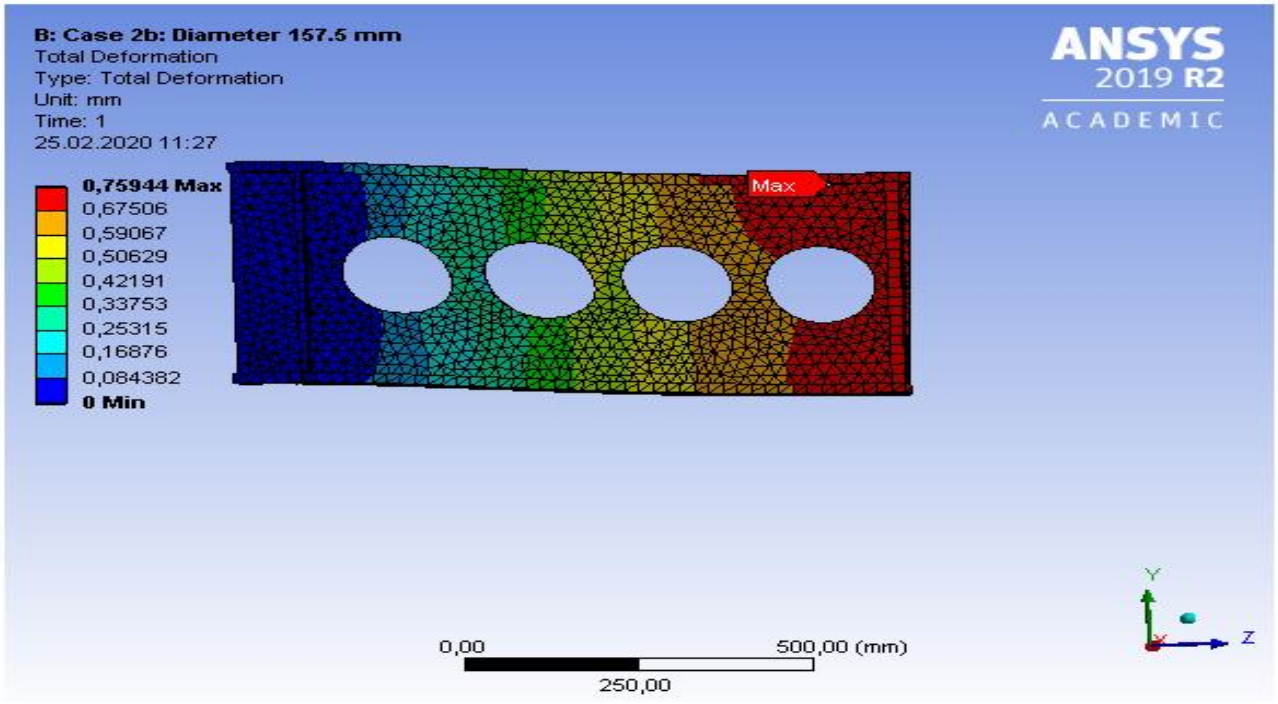

Figure 43 Deflection in case 2b

The maximum deflection is 0.76mm and is at the midspan as shown in the figure above.

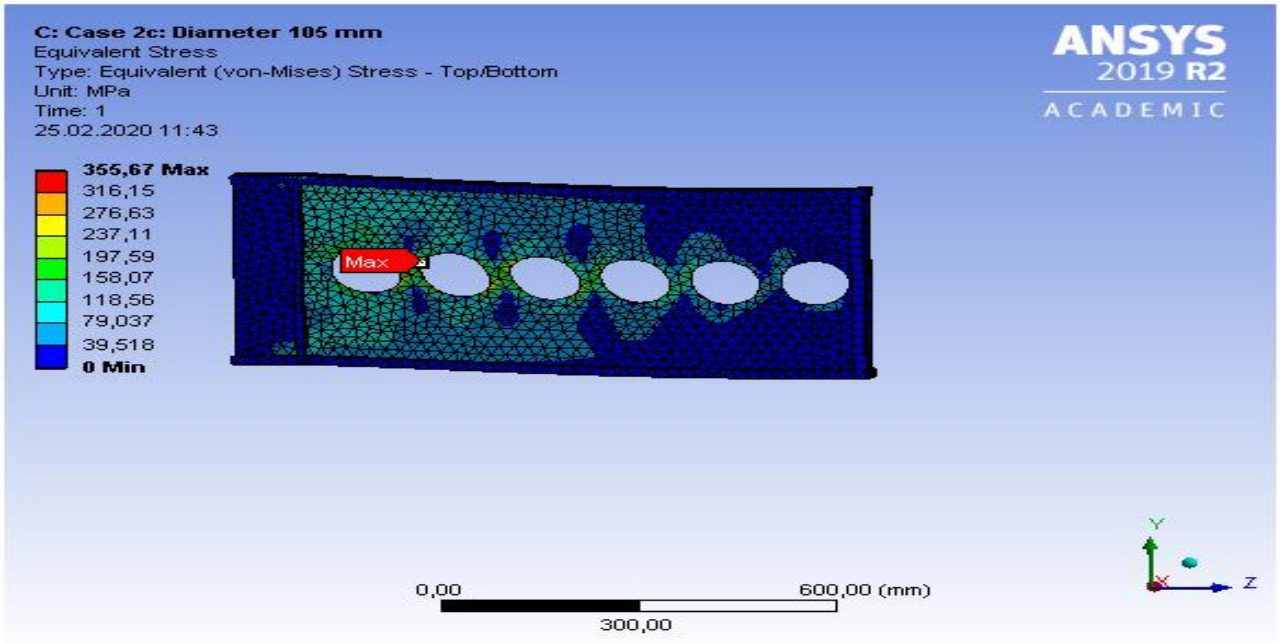

Figure 44 Von mises stress in case 2c

From the figure above the highest equivalent stress is around the web opening.

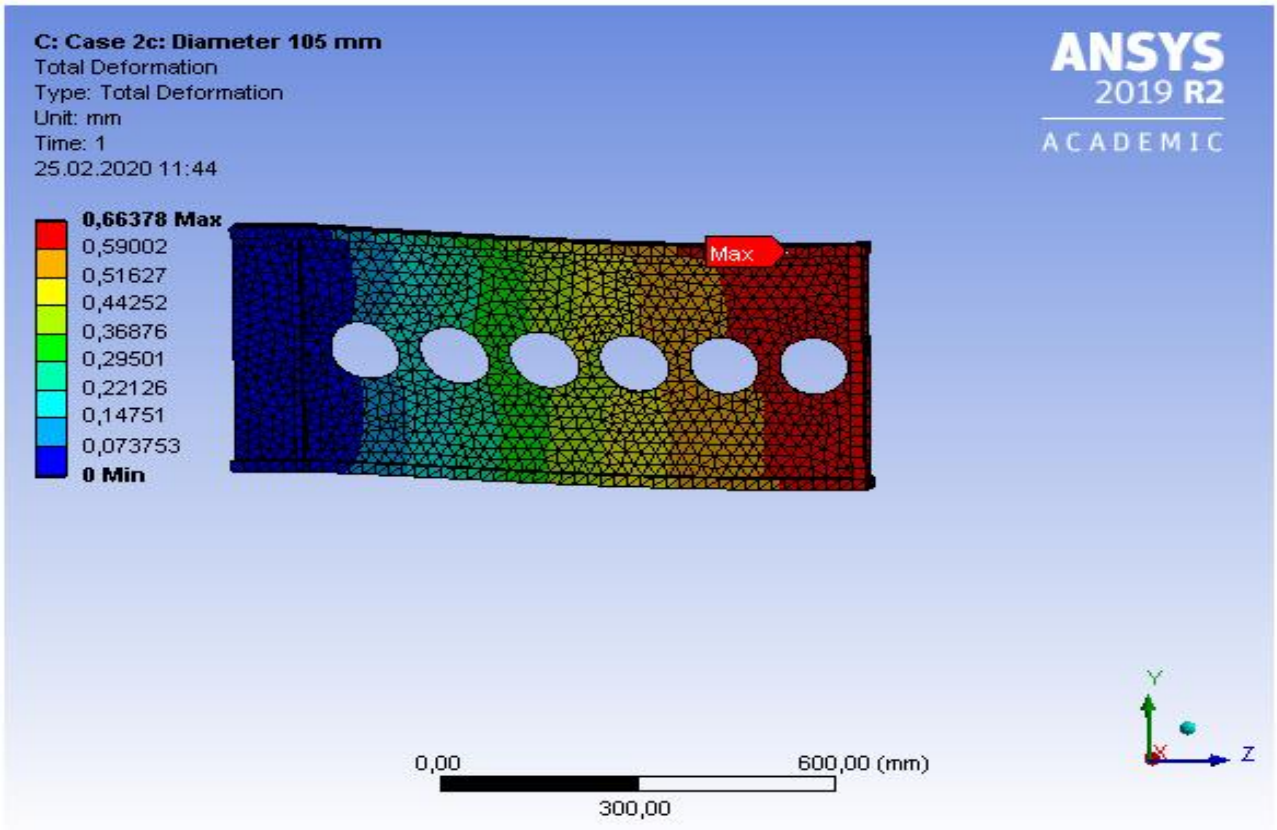

Figure 45 Deflection in case 2c

The deflection decreases further in case 2c due to the reduction in the opening diameter as shown in the figure above.

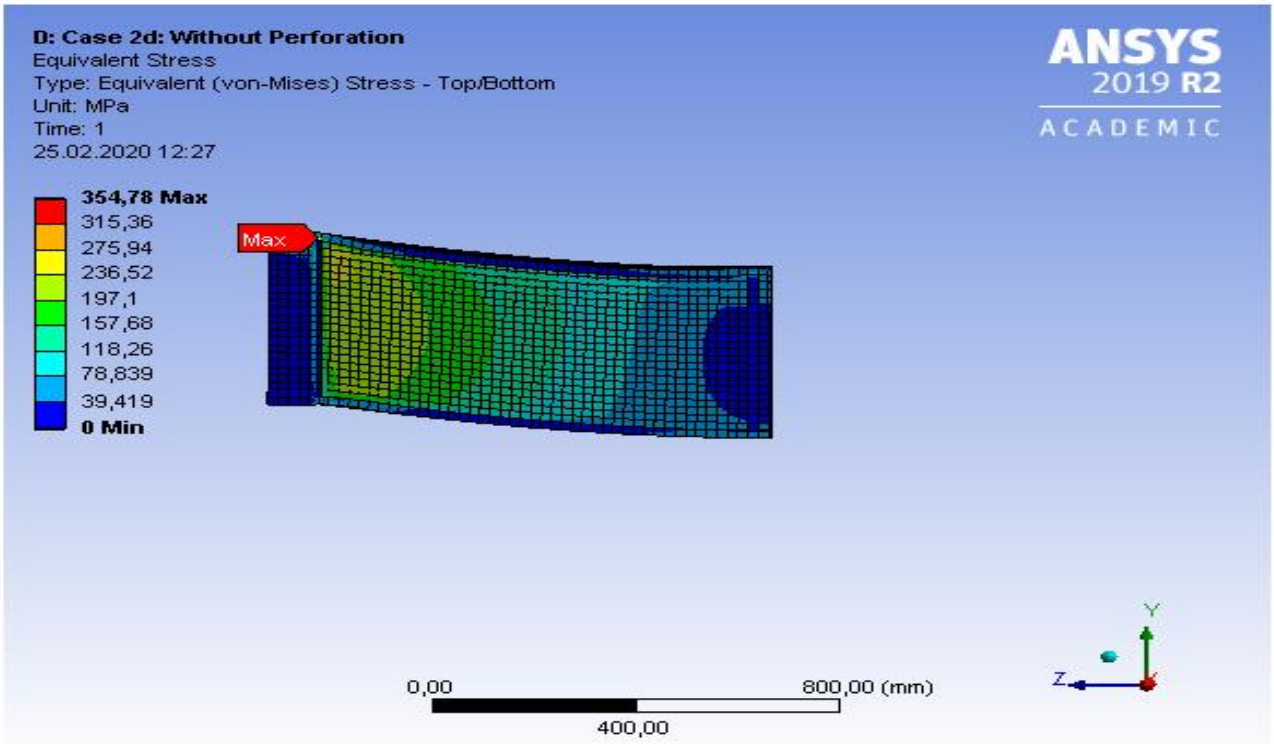

Figure 46 Von mises stress in case 2d

In subcase 2d which is the beam without perforation, the top flange buckles as illustrated in Figure 46.

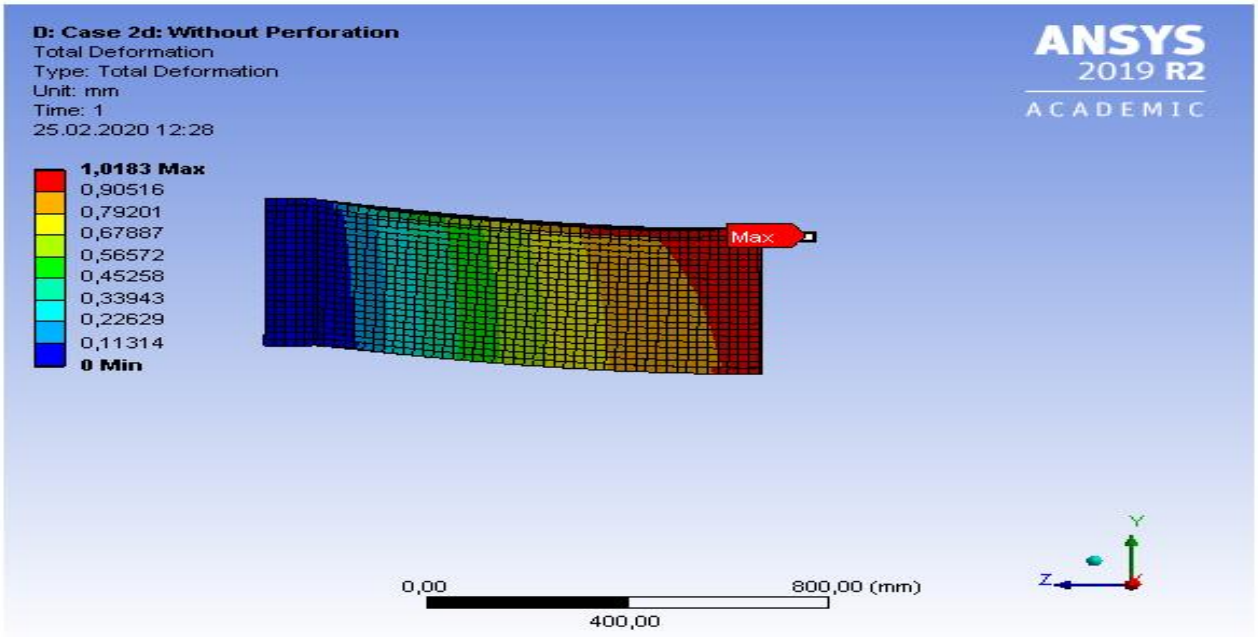

Figure 47 Deflection in case 2d

Figure 47 shows the maximum deflection of 1.01mm at the mid-span.

4.3 Case 3

Subcase 3a which is the optimal case in the simulations made in this thesis is shown in Table 6 among the other subcases in case 3. The web-post buckles in subcases a, b and c, and the top flange buckles in subcase d.

Table 6 Results from case 3

Subcase	Diameter [mm]	Yield load [kN]	Max. deflection [mm]	Failure mode
a	315	371	1.4	Web-post buckling
b	157.5	456	0.97	Web-post buckling
c	105	473.5	0.85	Web-post buckling
d	Without perforation	945	1.2	Top flange buckling

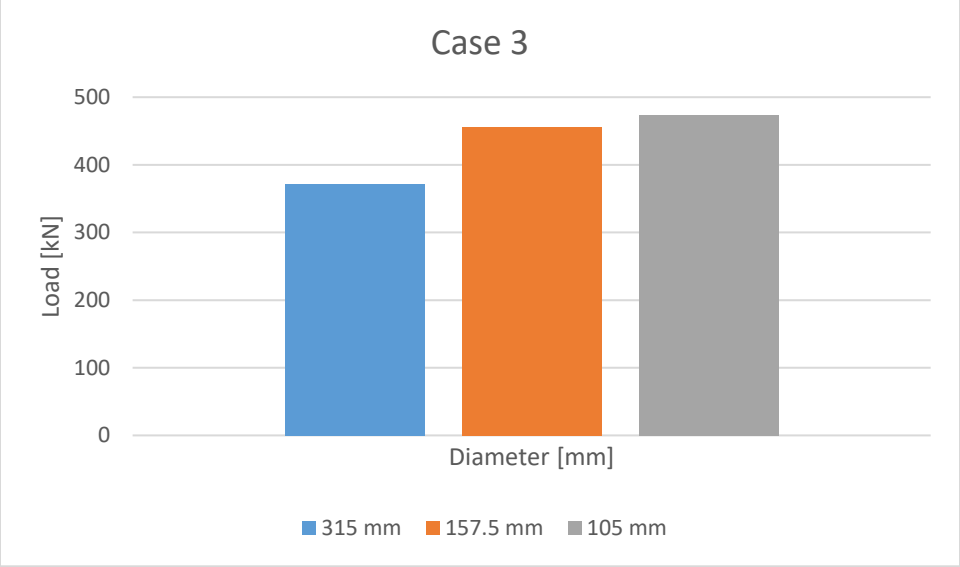

Figure 48 Load-diameter overview of case 3

When the opening diameter decreases, the load carrying capacity of the beam increases as shown in Figure 48.

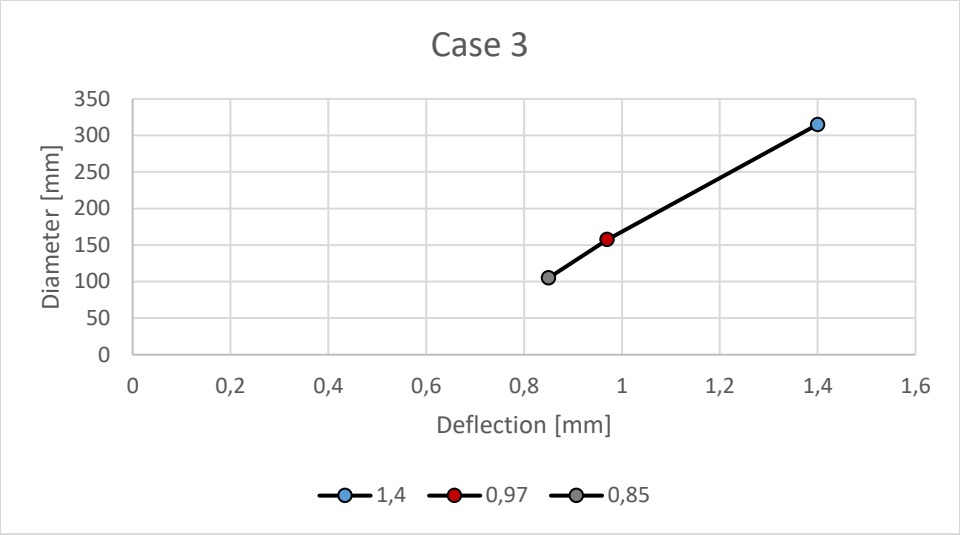

Figure 49 Diameter-deflection chart of case 3

Figure 49 shows the linear relation between the diameter and the deflection; the defection increases when the opening diameter increases.

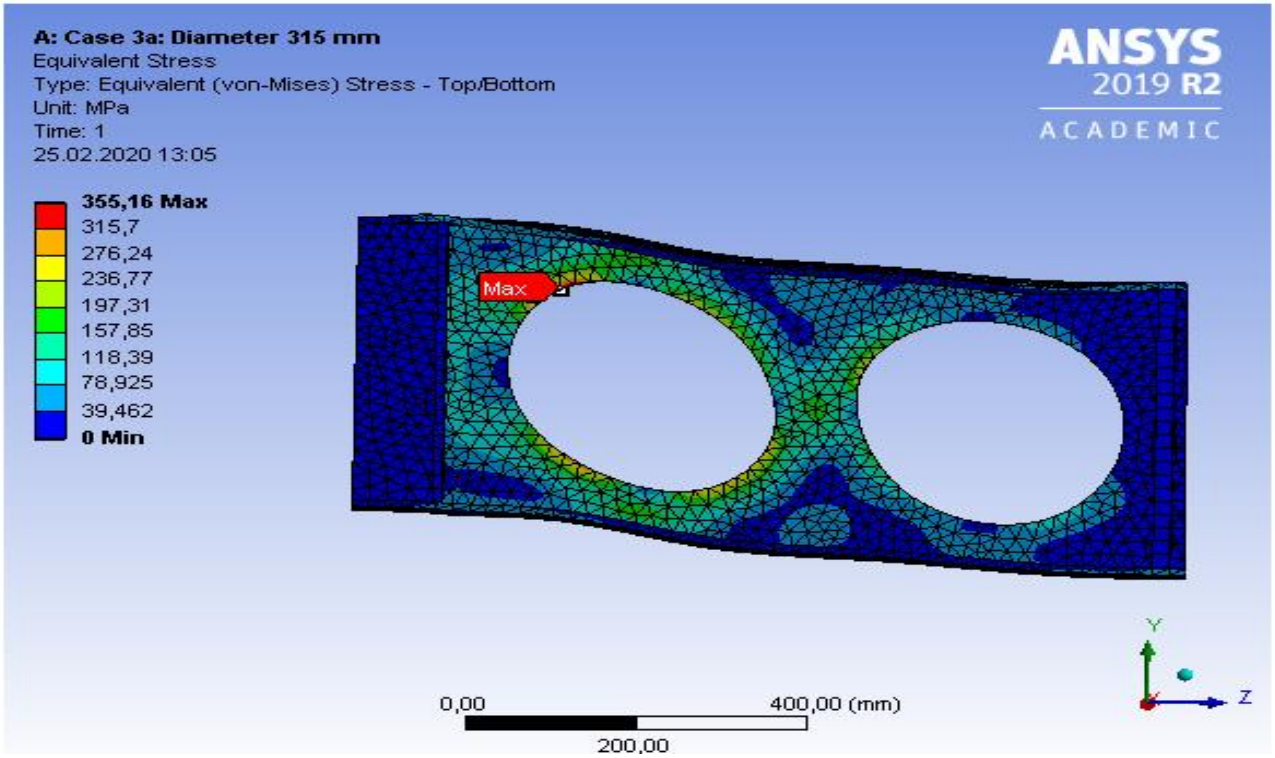

Figure 50 Von mises stress in case 3a

The highest stress is localized around the web opening. Figure 50 shows the left side of the symmetrical beam.

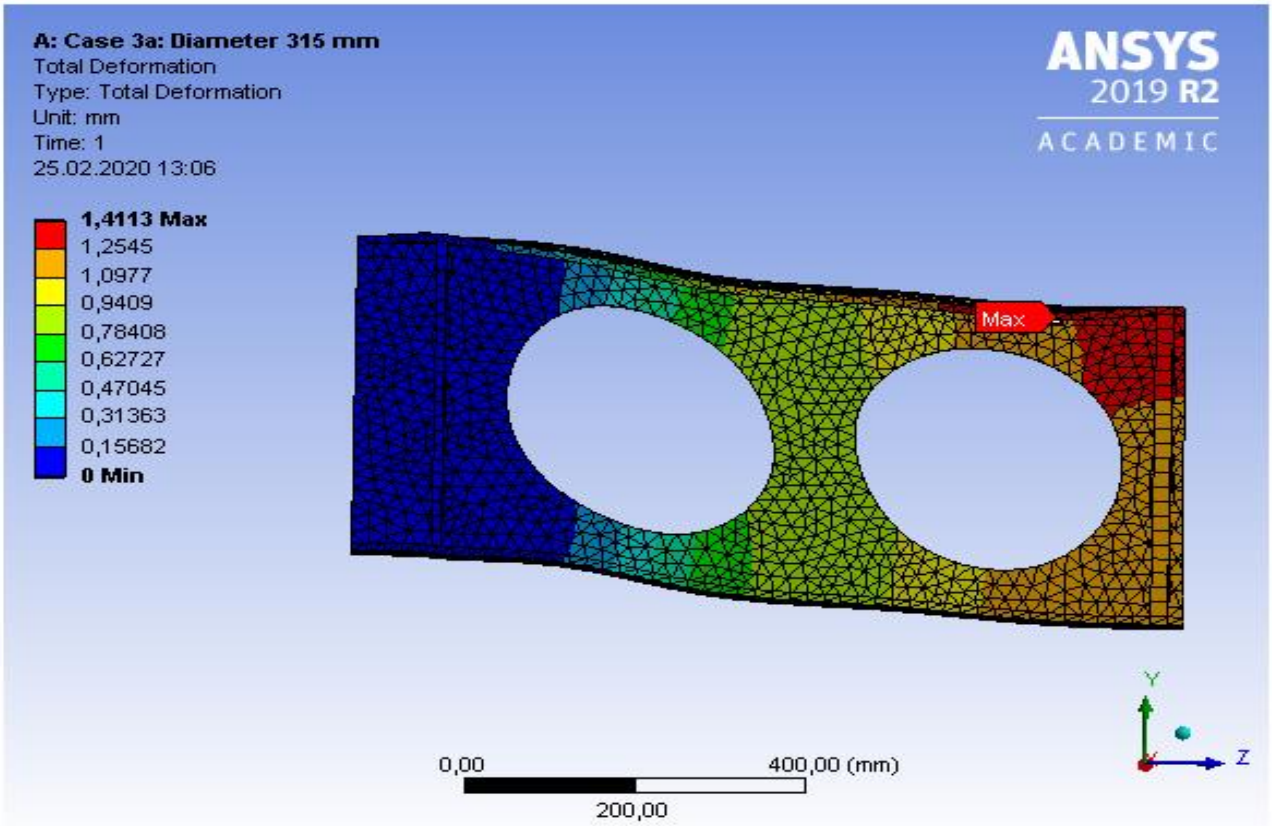

Figure 51 Deflection in case 3a

Figure 51 shows maximum deflection of 1.4mm at the mid-span for case 3a.

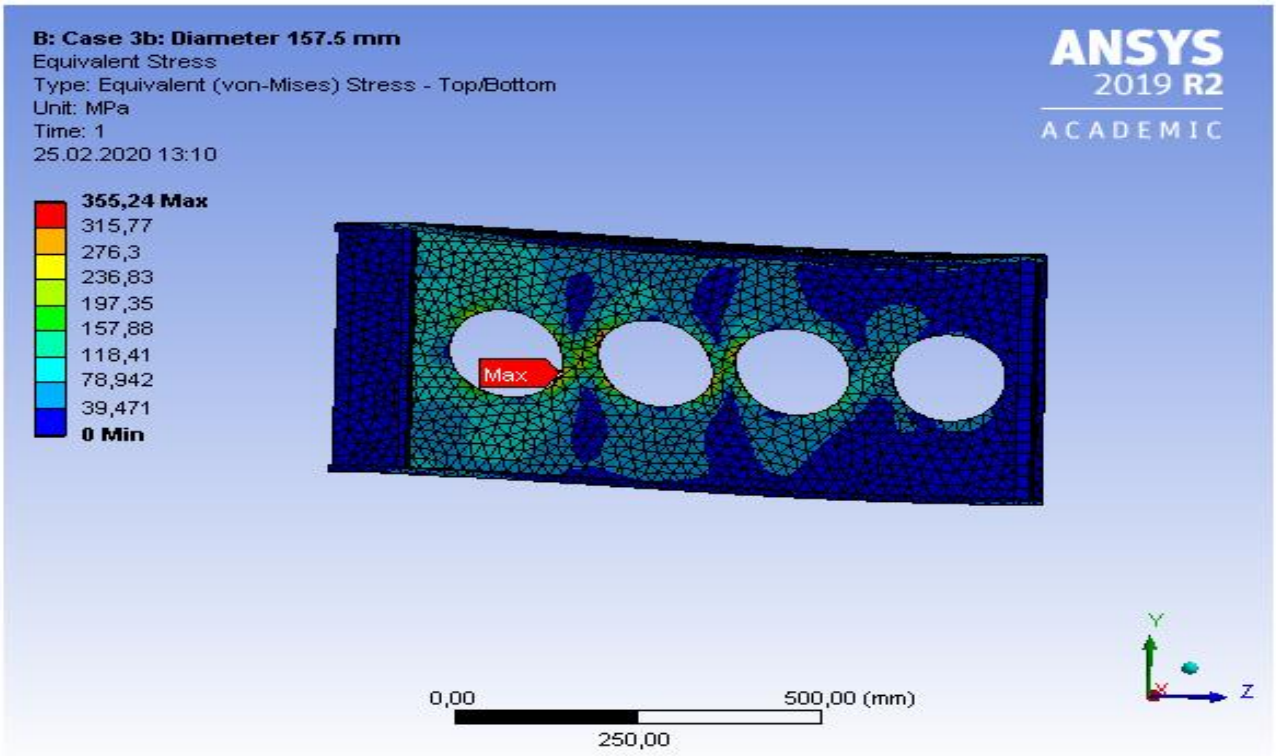

Figure 52 Von mises stress in case 3b

The decrease in the diameter results in an increase of number of holes in the web as shown in Figure 52. the maximum stress is around the web opening.

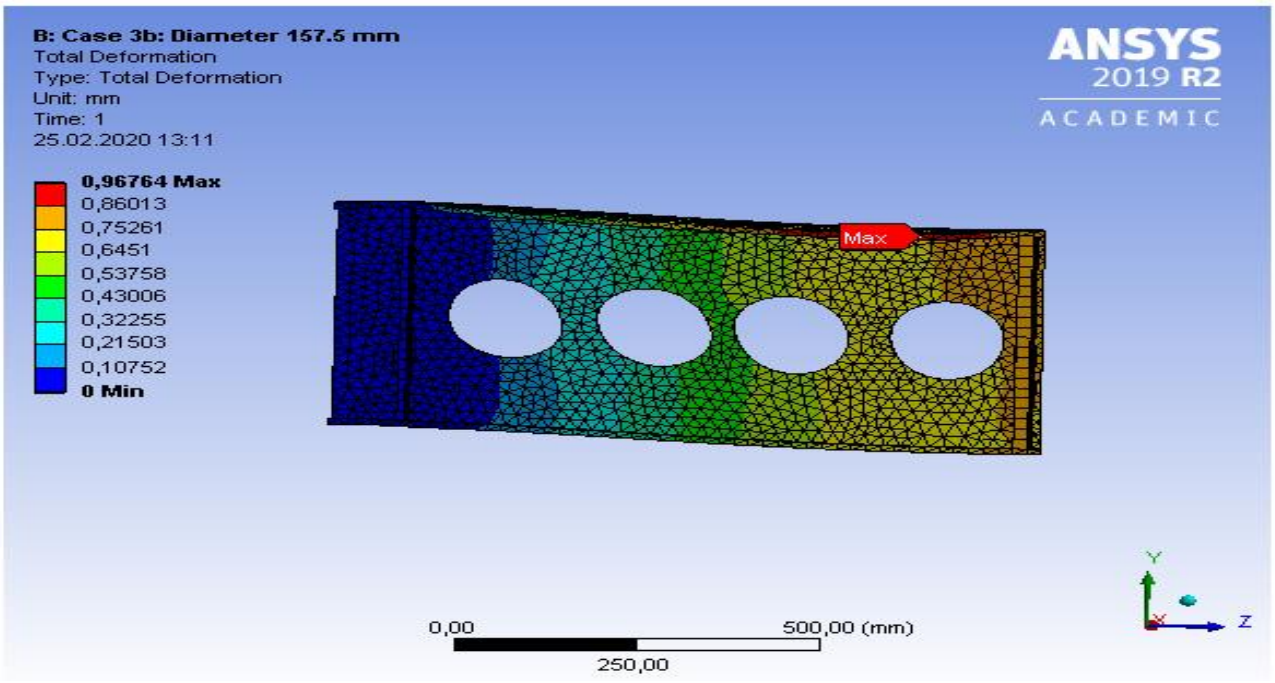

Figure 53 Deflection in case 3b

The deflection decreased significantly with the decrease of the diameter as shown in Figure 53.

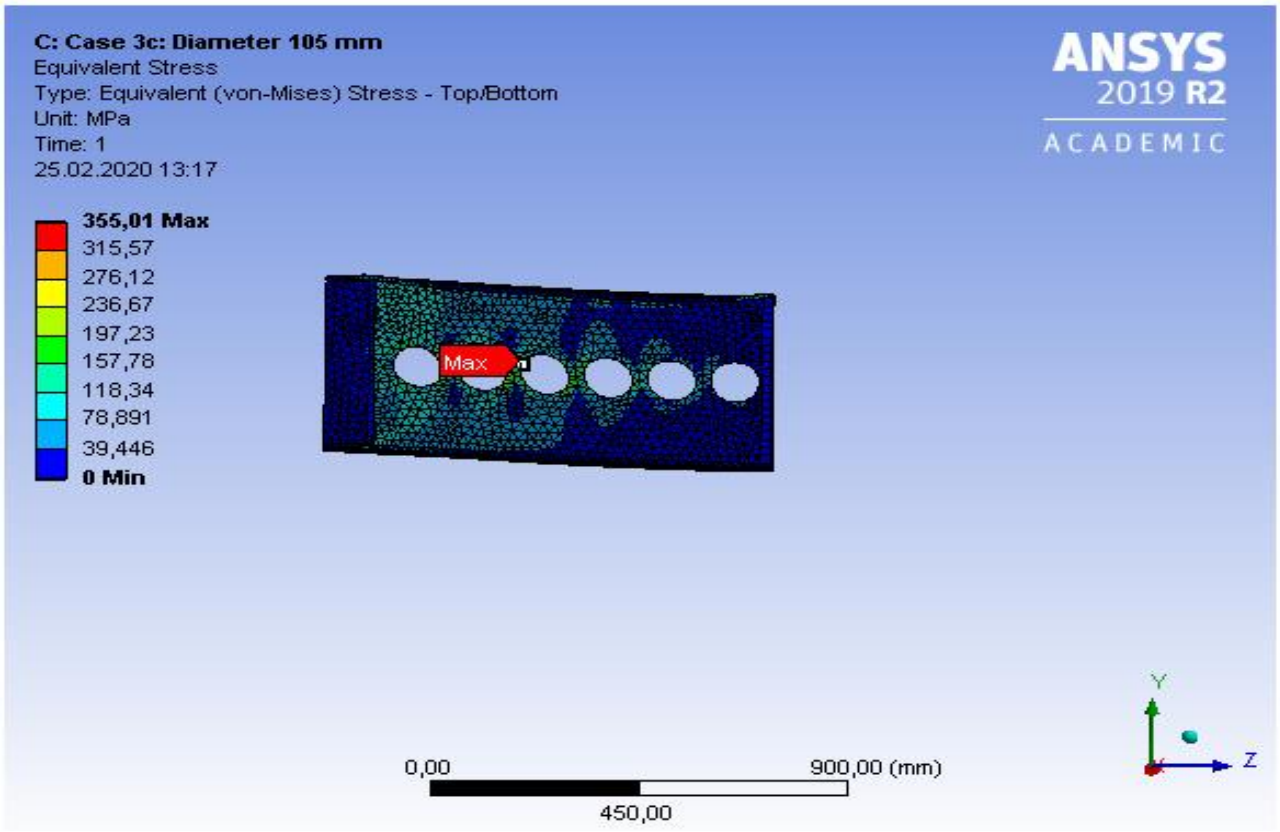

Figure 54 Von mises stress in case 3c

The maximum equivalent stress (Von mises stress) is acting around the web opening (see Figure 54), however the load bearing capacity of the web has increased with the reduction of the opening diameter.

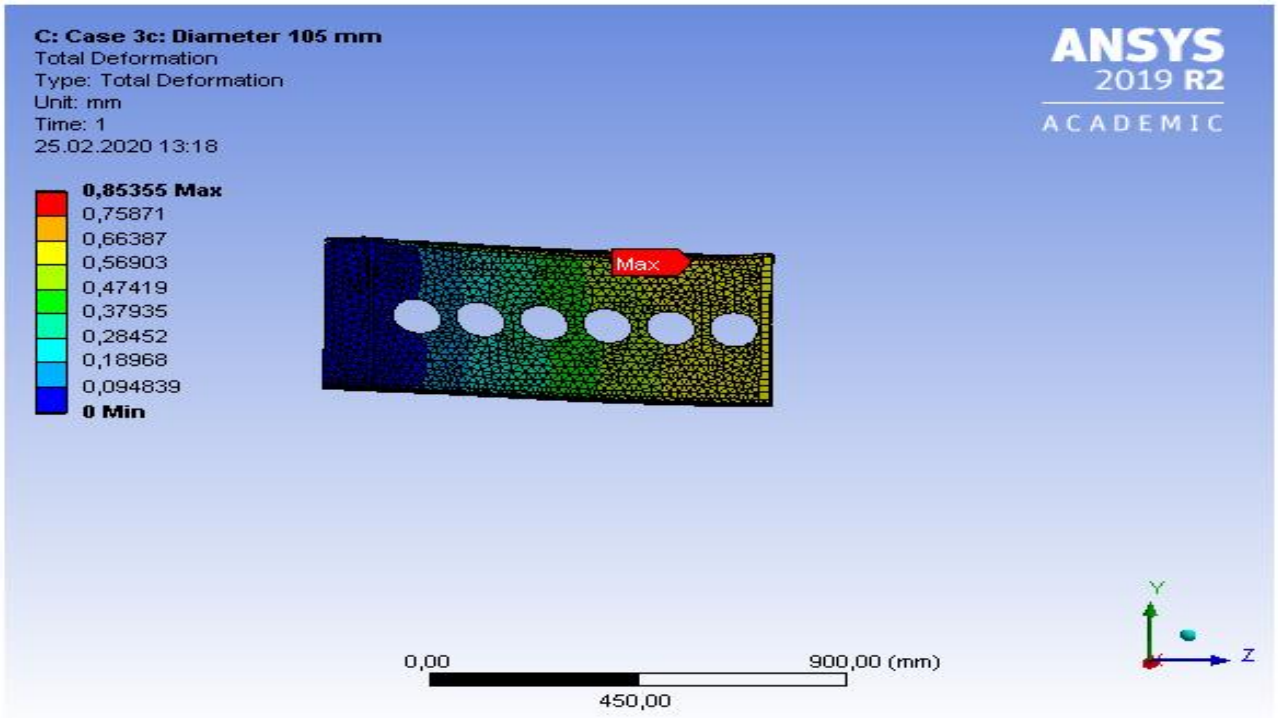

Figure 55 Deflection in case 3c

The deflection has decreased with the decrease in the opening diameter as show in the figure above.

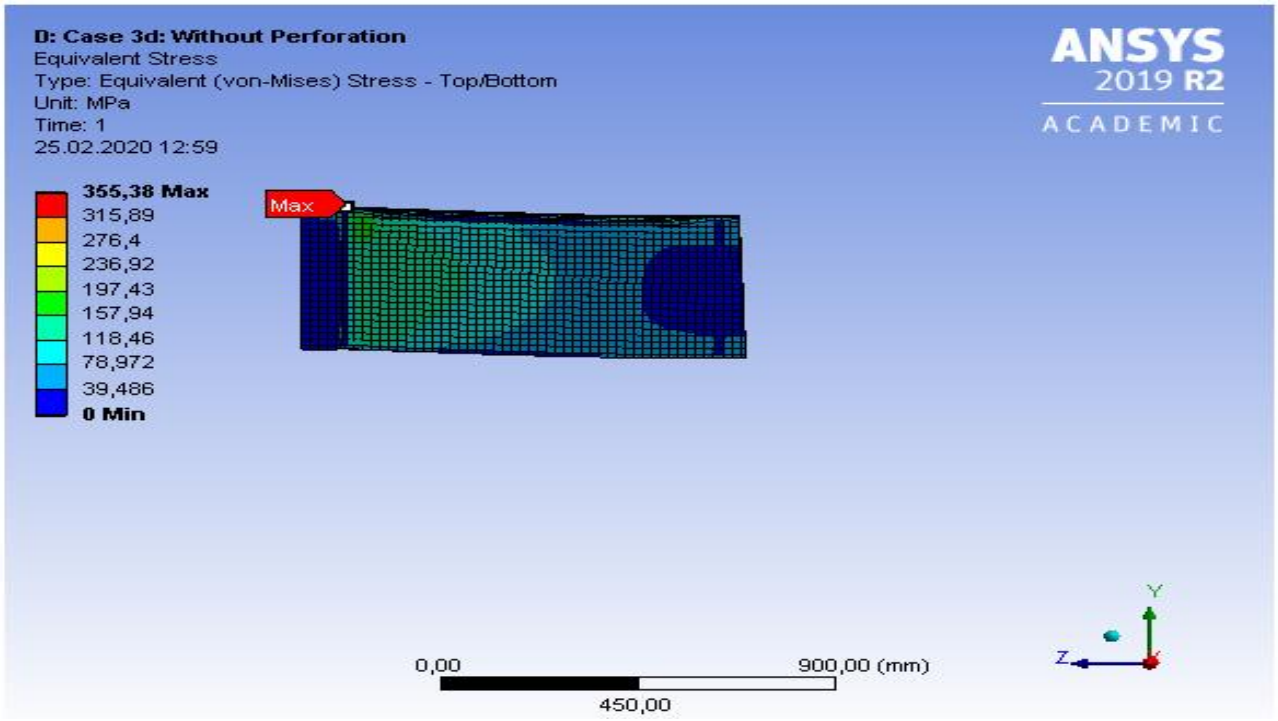

Figure 56 Von mises stress in case 3d

Subcase 1d has a different failure mode than the other cases. The top flange buckles because it is the weakest part in the beam as shown in Figure 56.

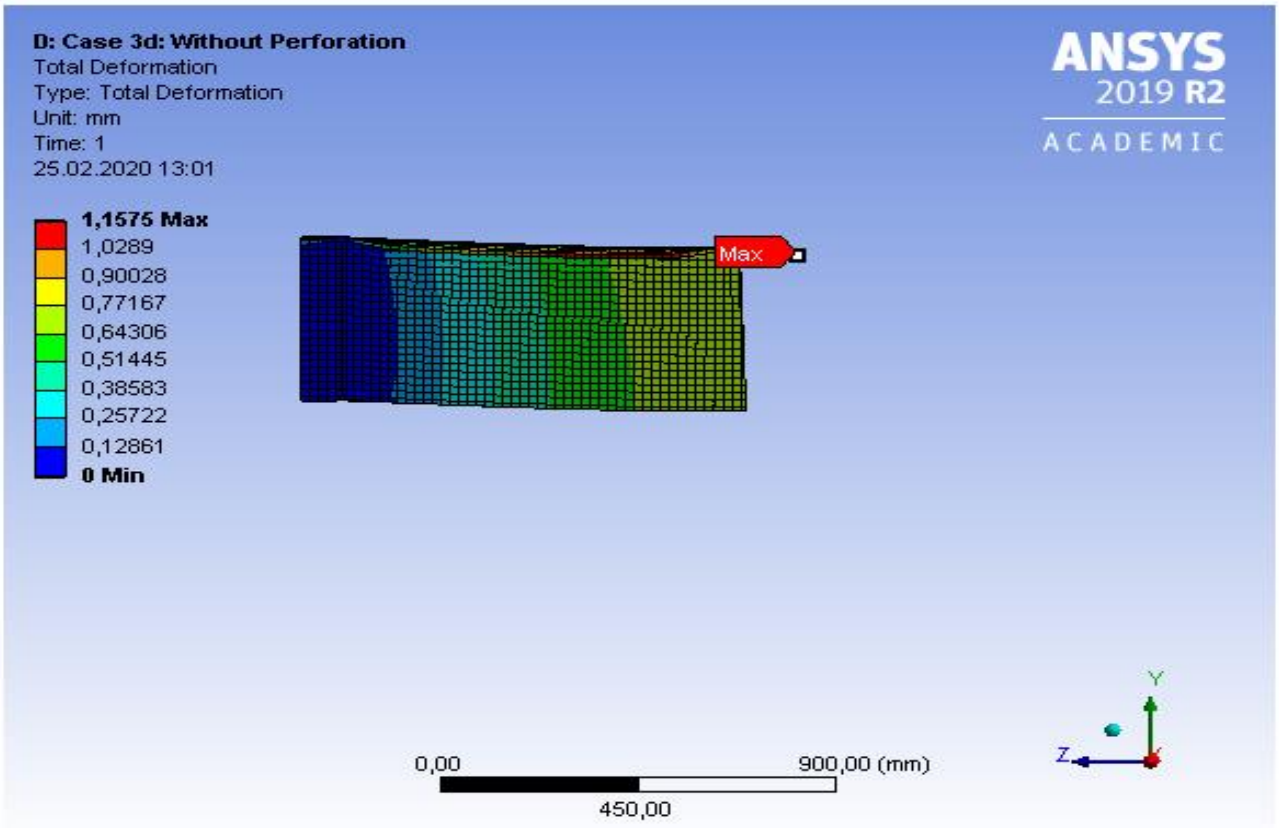

Figure 57 Deflection in case 3d

The maximum deflection in subcase 3d takes place at the top flange as shown in the figure above.

5 Discussion

5.1 Model validation

The aim of this thesis is to study the problem of steel beams with circular web openings numerically. Experimental results from testing series carried out by Tsavdaridis and Cedric D'Mello have been used to validate the proposed FEM simulations.

The shear web buckling strength obtained from FEM model concurred well with the test results, as shown in Table 1. The web-post yield strength from the FEM analysis is 255 kN in this thesis, while the one found in the test experiment was 250 kN. The difference is 2%. This shows the validity of the models used in the case analysis.

In order to maintain the same input data, the selection of steel section, mesh size, boundary conditions, and the rest of the parameters agreed to those of the research paper. Nevertheless, changes were made to three parameters; the diameter of the web openings, the thickness of the flanges and the thickness of the web.

The web opening spacing is based on the verified model's spacing criterion which is $1.3*d_0$, where d_0 is the diameter of the web opening. The diameter of the web opening in all cases is with reference to subcase 1a, which has opening/depth ratio of 0.7. The diameters of subcases b and subcase c are reduced by 50% and 66.7% respectively with reference to subcase 1a. As expected, the spacing between two openings decreases when the diameter of the opening becomes smaller.

To maintain the criterion of $1.3*d_0$, the number of web openings increases from 3 in subcase a to 8 and 12 in subcases b and c respectively.

Each parameter change increases the strength of the beam. This increase of strength is different in each case, but it is significant in every case.

Stiffeners are placed on the beam in order to prevent the buckling of the top flange before the web-post fails. Without the presence of these stiffeners, the flanges would have buckled thus making it impossible to measure the strength of the web-post.

5.2 Effects of the diameter of the web opening

In the first case study, the focus is placed on the variation of the diameter; the rest of the parameters are kept constant in agreement to the research paper. The results show that the shear capacity of the web-post has increased as the diameter of the opening decreases. Subcase 1a is the verified model.

As shown in Table 4, the shear capacity of the web-post has increased by 27% in case 1b, and further 35% in case 1c with respect to the reference case.

Case 1d is a special case, which is out of the scope of this analysis; however, this is included here only to see the capacity of the beam without perforation in relation to the perforated beam. The failure mode has changed in case 1d, since the weakest part of the element is the flange. In this case, failure occurs at the top flange in the form of buckling.

The deflection in general is not significant in all cases. However, it is observed that with the decrease in the diameter, there is also a decrease in the deflection of the beam. In case 1a, the deflection is 1.3mm. There is a decrease of 48% and 63% in subcases 1b and 1c respectively. In subcase 1d, the deflection is on the top flange and therefore cannot be compared with the perforated beam.

The main reason for minimal deflection on the beam is the support from the stiffeners, particularly the one that is placed in the middle of the beam where the load acts.

5.3 Effects of the flange thickness

The thickness of the flanges changed from 10.9 mm to 19.6 mm, which is the maximum production thickness of this section.

Comparison is made to the corresponding subcases in case 1. The variation in the flange thickness does increase significantly the shear capacity of the web-post as shown in Table 5. The web-post shear capacity is up by 4.3% in subcase 2a, 2% in subcase 2b and 3.2% in subcase 2c. The shear capacity of the web-post cannot be compared with perforated cases because of the failure mode difference as stated in point 5.2 above.

The deflection decreases 8.3% in case 2a, 16% in case 2b and 21.2% in case 2c.

5.4 Effects of the web thickness

The third parameter modified in this analysis is the web thickness. The thickness varied from 7.6mm to 11.4mm, the maximum production thickness of this section.

The results from the FEM model are compared to Case 1. The strength of the web-post has increased significantly as shown in Table 6. This happens since the web-post is strengthened.

The shear capacity of the web-post increased by 45.5% in subcase 3a, 41% in subcase 3b and 38% in subcases 3c in respect to the reference case. In case 3d the web-post is not the weaker part of the beam but rather the flanges are the weakest thus failure takes place at the flange.

The deflection has increased 7.7% in case 3a, 10.2% in subcase 3b and 6.3% in 3c. Since there is no perforation in the web, the flanges are the weakest parts of the beam and the deflection occurs at the top flange in case 3d.

5.5 Summary of the case studies and recommendations

Case 3a is the optimal case, which gives the highest strength to the beam as illustrated in Table 7. The increase in the web thickness increases the shear capacity of the web-post by 45.5% which is the maximum increase found in the results.

Table 7 Summary of shear capacity of the web-post in the cases analyzed

Case	Web-post shear capacity [kN]	% increase
1a	255	-
1b	324,5	-
1c	343	-
2a	266	4.3 %
2b	331	2.0 %
2c	354	3.2 %
3a	**371**	**45.5 %**
3b	456	40.5 %
3c	473,5	38.0 %

6 Conclusions

The main conclusions that can be derived from the analysis are the following:

- In general, deflection in steel cellular beams with stiffeners is not used as the design criterion for these types of steel beams.
- Increasing the thickness of the flanges does not contribute significantly to the increase of the capacity of the web-post. However, the deflection of the beam decreases due to the higher moment of inertia of the beam.
- The shear capacity of the web increases when the web becomes thicker.
- Cellular beams are practically used for long spans of more than 12m. This is the span limit where the cellular beams become more advantageous over regular solid beams.
- The presence of stiffeners is highly recommended since it has been proven to prevent Vierendeel bending failure mode of the tee sections.
- The main failure mode of the cellular beam is the web-post buckling.
- The stress is concentrated around the web openings since this area is the weakest part of the cellular beam.

7 Proposal for future research

The parts that require further research are the following:

- It is highly recommended to perform more experimental tests to consolidate the results from the finite element analysis, especially the effect of web thickness on the strength of the beam.
- An interesting field of research would be to investigate the interaction of cellular beams with different types of connections.
- The effect of varying the position of stiffeners on the strength of the beam must be further studied.
- The investigation of the plastic behavior of the cellular beam is highly recommended.

8 Bibliography

ANSYS Inc. (2017). *ANSYS Mechanical APDL Contact Technology Guide ANSYS,*. Available at: https://www.academia.edu/38866112/ANSYS_Mechanical_APDL_Contact_Technology_Guide?auto=download (accessed: 25.04-2020).

ANSYS Workbench. (2019). *2019 R2 ACADEMIC*. Available at: https://ansyshelp.ansys.com/account/secured?returnurl=/Views/Secured/corp/v194/ans_elem/Hlp_E_SOLID185.html.

Bresser, D., Ravenshorst, G. J. P. & Hoogenboom, P. C. J. (2020). General formulation of equivalent moment factor for elastic lateral torsional buckling of slender rectangular sections and I-sections. *Engineering Structures*, 207: 12. doi: 10.1016/j.engstruct.2020.110230.

British Constructional Steelwork Association. (2020). *Steel manufacture*. Available at: https://www.steelconstruction.info/Steel_manufacture (accessed: 27.02.2020).

Buildington database. (2011). *Palestra House*. Available at: https://www.buildington.co.uk/london-se1/197-blackfriars-road/palestra/id/2922 (accessed: 24.04.2020).

Cellbeam Ltd. (2019). *Cellular beams*. Available at: https://www.cellbeam.co.uk/ (accessed: 16.04.2020).

Chen, Y. Y., Cheng, X. & Nethercot, D. A. (2013). An overview study on cross-section classification of steel H-sections. *Journal of Constructional Steel Research*, 80: 386-393. doi: 10.1016/j.jcsr.2012.10.006.

Constructalia, A. E. (2007). *KEA Commercial Centre, Cyprus*. Available at: https://constructalia.arcelormittal.com/en/case_study_gallery/cyprus/ikea_commercial_centre_cyprus_visible_steel_structure_with_longspan_acb_beams (accessed: 25.04.2020).

EC3-1-1. (2005). *Eurocode 3: Design of steel structures*. Part 1-1: General rules and rules for buildings: CEN - European Committee for Standardization.

Erdal, F., Dogan, E. & Saka, M. P. (2011). Optimum design of cellular beams using harmony search and particle swarm optimizers. *Journal of Constructional Steel Research*, 67 (2): 237-247. doi: 10.1016/j.jcsr.2010.07.014.

Fares, S. S., Coulson, J. & Dinehart, D. W. (2016). *Castellated and cellular beam design*. Steel design guide 31. Chicago: American Institute of Steel Construction.

Kittur, M. & Huston, R. (1989). Mesh refinement in finite element analysis by minimization of the stiffness matrix trace.

Klaus-Jürgen Bathe. (2014). *Finite Element Procedures*. 2. ed. New Jersey: Prentice Hall, Pearson Education, Inc.

Larsen, P. K. (2010). *Dimensjonering av stålkonstruksjoner*. 2. ed. Bergen: Fagbokforlaget.

Lida Group. (2013). *Continuous frames*. Available at: http://www.lidajituan.com/en/news/02/3253.html (accessed: 25.04.2020).

Macsteel Service Centers SA. (2019). *Cellular Beams*. Available at: https://macsteel.co.za/downloads/ (accessed: 10.03.2020).

Müller, D.-I. C. & Oppe, D.-I. M. (2008). *Conceptual design and design examples for multi-storey buildings*. Brussels: RWTH Aachen.

New Steel Construction Magazine. (2019). *An introduction to cellular beams*. Available at: https://www.newsteelconstruction.com/wp/an-introduction-to-cellular-beams/ (accessed: 19.03.2020).

Nikishkov, G. (2004). Introduction to the finite element method. *University of Aizu*: 1-70.

Panedpojaman, P., Thepchatri, T. & Limkatanyu, S. (2014). Novel design equations for shear strength of local web-post buckling in cellular beams. *Thin-Walled Structures*, 76: 92-104. doi: 10.1016/j.tws.2013.11.007.

Panedpojaman, P., Thepchatri, T. & Limkatanyu, S. (2015). Novel simplified equations for Vierendeel design of beams with (elongated) circular openings. *Journal of Constructional Steel Research*, 112: 10-21. doi: 10.1016/j.jcsr.2015.04.007.

Recycling Magazine. (2019). *Crude steel production decreased in October*. Available at: https://www.recycling-magazine.com/2019/11/26/crude-steel-production-decreased-in-october/#. (accessed: 08.03.2020).

Reliance Foundry. (2020). *Hot Rolled vs Cold Rolled Steel*. Available at: https://www.reliance-foundry.com/blog/hot-vs-cold-rolled-steel#gref (accessed: 03.03.2020).

Sebastien, D., AbdelHamid, B. & Olivier, V. (2013). Validation of an analytical model for curved and tapered cellular beams at normal and fire conditions. *Periodica Polytechnica-Civil Engineering*, 57 (1): 83-95. doi: 10.3311/PPci.2144.

Simscale. (2020). *Finite Element Analysis*. Available at: https://www.simscale.com/docs/content/simwiki/fea/what-is-von-mises-stress.html (accessed: 23.03.2020).

Tsavdaridis, K. D. & D'Mello, C. (2011). Web buckling study of the behaviour and strength of perforated steel beams with different novel web opening shapes. *Journal of Constructional Steel Research*, 67 (10): 1605-1620. doi: 10.1016/j.jcsr.2011.04.004.

Case 3a

Project*

Author	Abdimalik Sheikh Muhumed
Subject	Elastic analyses
Prepared for	Master's Thesis-NMBU
First Saved	Wednesday, February 12, 2020
Last Saved	Thursday, April 23, 2020
Product Version	2019 R3
Save Project Before Solution	No
Save Project After Solution	No

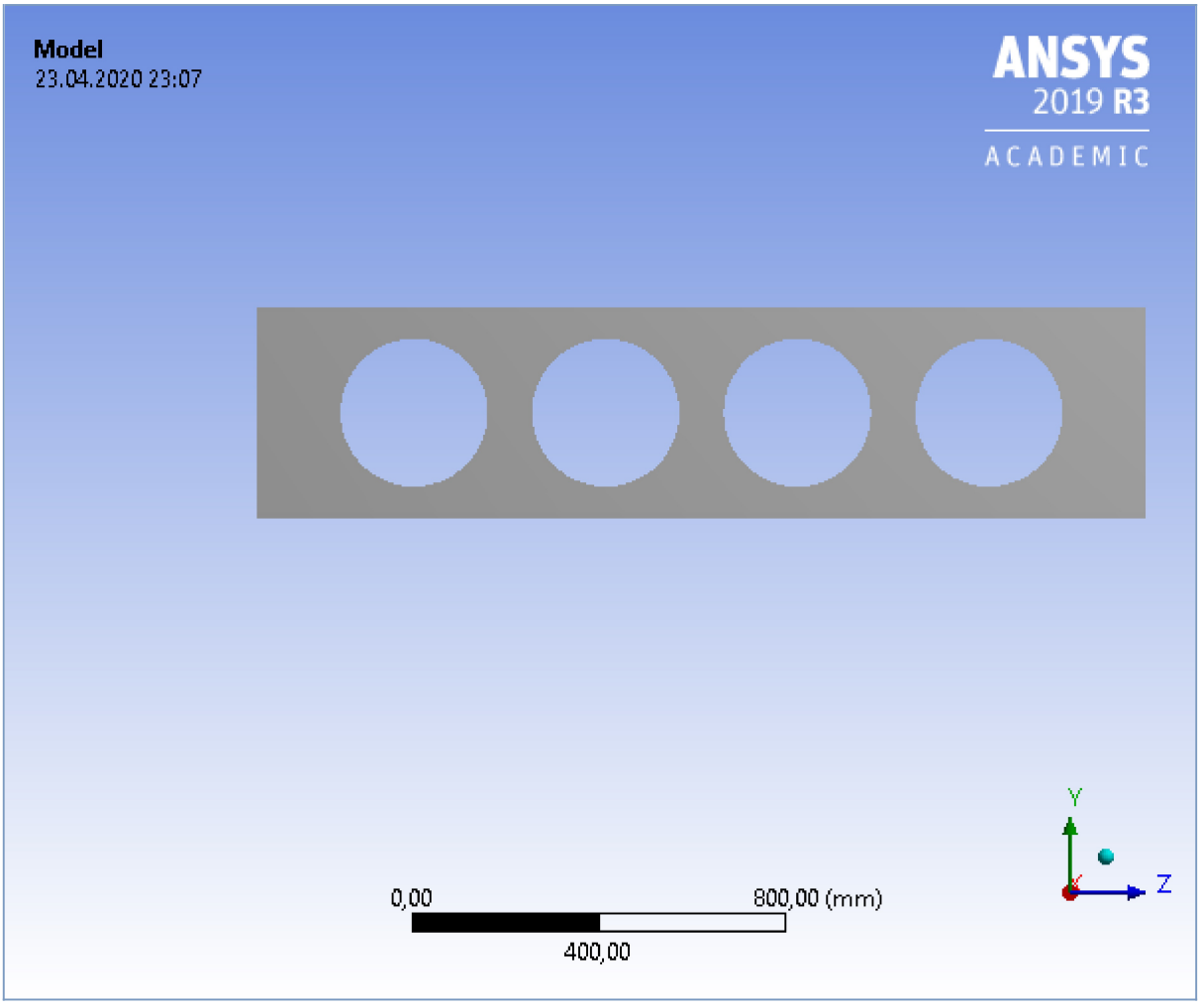

Contents

Units

TABLE 1

Unit System	Metric (mm, kg, N, s, mV, mA) Degrees rad/s Celsius
Angle	Degrees
Rotational Velocity	rad/s
Temperature	Celsius

Model (A4)

Geometry

TABLE 2
Model (A4) > Geometry

Object Name	*Geometry*
State	Fully Defined
Definition	
Source	C:\Users\Hp\Dropbox\Master Thesis Abdimalik\ANSYS MODEL\Case 3_files\dp0\SYS-1\DM\SYS-1.agdb
Type	DesignModeler
Length Unit	Meters
Element Control	Program Controlled
Display Style	Body Color
Bounding Box	
Length X	156,2 mm
Length Y	449,8 mm
Length Z	1900, mm
Properties	
Volume	1,462e+007 mm³

Mass	114,77 kg
Scale Factor Value	1,
Statistics	
Bodies	7
Active Bodies	7
Nodes	36170
Elements	17582
Mesh Metric	None
Update Options	
Assign Default Material	No
Basic Geometry Options	
Parameters	Independent
Parameter Key	
Attributes	Yes
Attribute Key	
Named Selections	Yes
Named Selection Key	
Material Properties	Yes
Advanced Geometry Options	
Use Associativity	Yes
Coordinate Systems	Yes
Coordinate System Key	
Reader Mode Saves Updated File	No
Use Instances	Yes
Smart CAD Update	Yes
Compare Parts On Update	No
Analysis Type	3-D
Clean Bodies On Import	No
Stitch Surfaces On Import	None
Decompose Disjoint Geometry	Yes
Enclosure and Symmetry Processing	Yes

TABLE 3
Model (A4) > Geometry > Parts

Object Name	*Solid*	*Surface Body*	*Surface Body*	*Surface Body*	*Surface Body*	*Surface Body*	*Surface Body*
State	Meshed						
Graphics Properties							
Visible	Yes						
Transparency	1						
Definition							
Suppressed	No						
Stiffness Behavior	Flexible						
Coordinate System	Default Coordinate System						
Reference Temperature	By Environment						
Treatment	None						
Dimension		3D					
Thickness		20, mm	10,9 mm		20, mm		10,9 mm
Thickness Mode		Manual					
Offset Type		Middle					
Material							
Assignment	Structural Steel						
Nonlinear Effects	Yes						

Thermal Strain Effects	Yes					
Bounding Box						
Length X	152,4 mm	72,4 mm				
Length Y	449,8 mm	428, mm				
Length Z	1900, mm	0, mm				
Properties						
Volume	1,2029e+007 mm³	6,1974e+005 mm³	3,3776e+005 mm³		6,1974e+005 mm³	3,3776e+005 mm³
Mass	94,429 kg	4,865 kg	2,6514 kg		4,865 kg	2,6514 kg
Centroid X	9,2739e-015 mm	-41,9 mm			41,9 mm	
Centroid Y	224,9 mm					
Centroid Z	-950, mm		-1800, mm	-100, mm	-950, mm	-1800, mm / -100, mm
Moment of Inertia Ip1	3,4137e+007 kg·mm²	74266 kg·mm²	40475 kg·mm²		74266 kg·mm²	40475 kg·mm²
Moment of Inertia Ip2	3,0907e+007 kg·mm²	2125,1 kg·mm²	1158,2 kg·mm²		2125,1 kg·mm²	1158,2 kg·mm²
Moment of Inertia Ip3	3,4229e+006 kg·mm²	76391 kg·mm²	41633 kg·mm²		76391 kg·mm²	41633 kg·mm²
Surface Area (approx.)		30987 mm²				
Statistics						
Nodes	35510	110				
Elements	17078	84				
Mesh Metric	None					
CAD Attributes						
DMSheetThickness		0,02	0,0109		0,02	0,0109

TABLE 4
Model (A4) > Materials

Object Name	*Materials*
State	Fully Defined
Statistics	
Materials	1
Material Assignments	0

TABLE 5
Model (A4) > Cross Sections

Object Name	*Cross Sections*
State	Fully Defined
Statistics	
Cross Sections	1

TABLE 6
Model (A4) > Cross Sections > I1

Object Name	*I1*
State	Fully Defined
Dimensions	
W1	152,4 mm
W2	152,4 mm
W3	449,8 mm
t1	10,9 mm
t2	10,9 mm
t3	11,4 mm
Physical Properties	
Beam Section	I1

Type	I
A	8201,5 mm²
Iyy	2,3451e+008 mm²·mm²
Izz	6,4831e+006 mm²·mm²

Coordinate Systems

TABLE 7
Model (A4) > Coordinate Systems > Coordinate System

Object Name	*Global Coordinate System*
State	Fully Defined
Definition	
Type	Cartesian
Coordinate System ID	0,
Origin	
Origin X	0, mm
Origin Y	0, mm
Origin Z	0, mm
Directional Vectors	
X Axis Data	[1, 0, 0,]
Y Axis Data	[0, 1, 0,]
Z Axis Data	[0, 0, 1,]

Connections

TABLE 8
Model (A4) > Connections

Object Name	*Connections*
State	Fully Defined
Auto Detection	
Generate Automatic Connection On Refresh	Yes
Transparency	
Enabled	Yes

TABLE 9
Model (A4) > Connections > Contacts

Object Name	*Contacts*	*Contacts 2*
State	Fully Defined	
Definition		
Connection Type	Contact	
Scope		
Scoping Method	Geometry Selection	
Geometry	All Bodies	
Auto Detection		
Tolerance Type	Slider	
Tolerance Slider	0,	
Tolerance Value	4,8969 mm	
Use Range	No	
Face/Face	No	
Face/Edge	No	
Edge/Edge	No	
Priority	Include All	
Group By	Bodies	
Search Across	Bodies	
Statistics		
Connections	0	2

Active Connections	0	2

TABLE 10
Model (A4) > Connections > Contacts 2 > Contact Regions

Object Name	*Bonded - Multiple To Solid*	*Bonded - Multiple To Solid*
State	Fully Defined	
Scope		
Scoping Method	Geometry Selection	
Contact	9 Edges	
Target	3 Faces	
Contact Bodies	Multiple	
Target Bodies	Solid	
Shell Thickness Effect	No	
Protected	No	
Definition		
Type	Bonded	
Scope Mode	Manual	
Trim Contact	Program Controlled	
Suppressed	No	
Advanced		
Formulation	Program Controlled	
Small Sliding	Program Controlled	
Penetration Tolerance	Program Controlled	
Elastic Slip Tolerance	Program Controlled	
Normal Stiffness	Program Controlled	
Update Stiffness	Program Controlled	
Pinball Region	Program Controlled	
Geometric Modification		
Target Geometry Correction	None	

Mesh

TABLE 11
Model (A4) > Mesh

Object Name	*Mesh*
State	Solved
Display	
Display Style	Use Geometry Setting
Defaults	
Physics Preference	Mechanical
Element Order	Program Controlled
Element Size	20, mm
Sizing	
Use Adaptive Sizing	No
Use Uniform Size Function For Sheets	No
Growth Rate	Default (1,2)
Max Size	Default (20, mm)
Mesh Defeaturing	Yes
Defeature Size	Default (0,1 mm)
Capture Curvature	Yes
Curvature Min Size	Default (0,2 mm)
Curvature Normal Angle	Default (30,°)
Capture Proximity	No
Bounding Box Diagonal	1958,8 mm
Average Surface Area	94279 mm²
Minimum Edge Length	10,9 mm

Quality	
Check Mesh Quality	Yes, Errors
Error Limits	Standard Mechanical
Target Quality	Default (0.050000)
Smoothing	Medium
Mesh Metric	None
Inflation	
Use Automatic Inflation	None
Inflation Option	Smooth Transition
Transition Ratio	0,272
Maximum Layers	5
Growth Rate	1,2
Inflation Algorithm	Pre
View Advanced Options	No
Advanced	
Number of CPUs for Parallel Part Meshing	Program Controlled
Straight Sided Elements	No
Rigid Body Behavior	Dimensionally Reduced
Triangle Surface Mesher	Program Controlled
Topology Checking	Yes
Pinch Tolerance	Default (0,18 mm)
Generate Pinch on Refresh	No
Sheet Loop Removal	No
Statistics	
Nodes	36170
Elements	17582

FIGURE 1
Model (A4) > Mesh > Figure

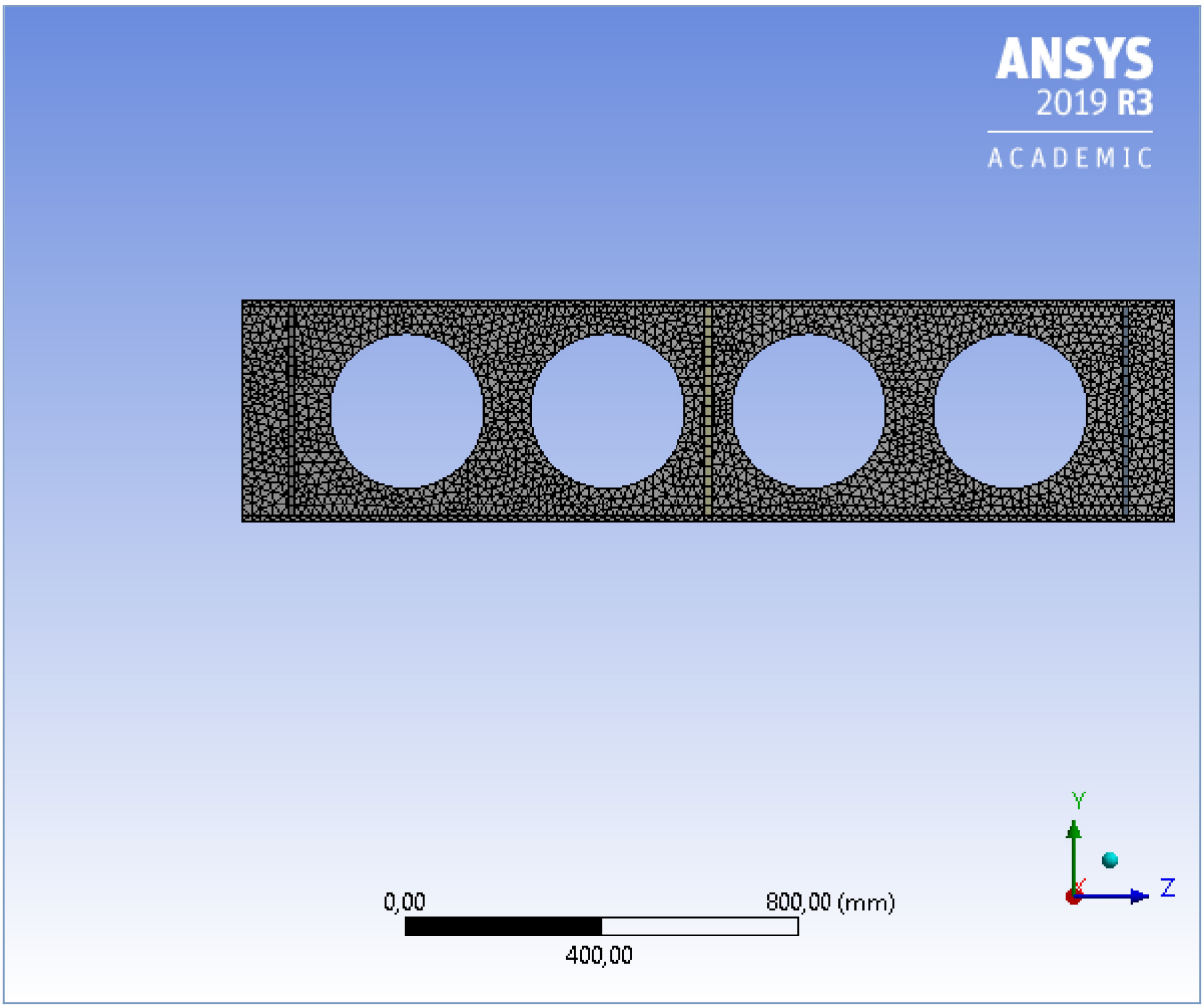

Static Structural (A5)

TABLE 12
Model (A4) > Analysis

Object Name	*Static Structural (A5)*
State	Solved
Definition	
Physics Type	Structural
Analysis Type	Static Structural
Solver Target	Mechanical APDL
Options	
Environment Temperature	22, °C
Generate Input Only	No

TABLE 13
Model (A4) > Static Structural (A5) > Analysis Settings

Object Name	*Analysis Settings*
State	Fully Defined
Step Controls	
Number Of Steps	1,
Current Step Number	1,
Step End Time	1, s
Auto Time Stepping	Program Controlled
Solver Controls	
Solver Type	Program Controlled
Weak Springs	Off

Solver Pivot Checking	Program Controlled
Large Deflection	Off
Inertia Relief	Off
Rotordynamics Controls	
Coriolis Effect	Off
Restart Controls	
Generate Restart Points	Program Controlled
Retain Files After Full Solve	No
Combine Restart Files	Program Controlled
Nonlinear Controls	
Newton-Raphson Option	Program Controlled
Force Convergence	Program Controlled
Moment Convergence	Program Controlled
Displacement Convergence	Program Controlled
Rotation Convergence	Program Controlled
Line Search	Program Controlled
Stabilization	Program Controlled
Advanced	
Inverse Option	No
Output Controls	
Stress	Yes
Surface Stress	No
Back Stress	No
Strain	Yes
Contact Data	Yes
Nonlinear Data	No
Nodal Forces	No
Contact Miscellaneous	No
General Miscellaneous	No
Store Results At	All Time Points
Result File Compression	Program Controlled
Analysis Data Management	
Solver Files Directory	C:\Users\Hp\Dropbox\Master Thesis Abdimalik\ANSYS MODEL\Case 3_files\dp0\SYS-1\MECH\
Future Analysis	None
Scratch Solver Files Directory	
Save MAPDL db	No
Contact Summary	Program Controlled
Delete Unneeded Files	Yes
Nonlinear Solution	No
Solver Units	Active System
Solver Unit System	nmm

TABLE 14
Model (A4) > Static Structural (A5) > Loads

Object Name	*Force*	*Fixed Support*	*Displacement*	*Fixed Support 2*
State	Fully Defined			
Scope				
Scoping Method	Geometry Selection			
Geometry	1 Face	1 Edge		12 Edges
Definition				
Type	Force	Fixed Support	Displacement	Fixed Support
Define By	Vector		Components	
Magnitude	3,71e+005 N (ramped)			

Direction	Defined		
Suppressed	No		
Coordinate System		Global Coordinate System	
X Component		0, mm (ramped)	
Y Component		0, mm (ramped)	
Z Component		Free	

FIGURE 2
Model (A4) > Static Structural (A5) > Force

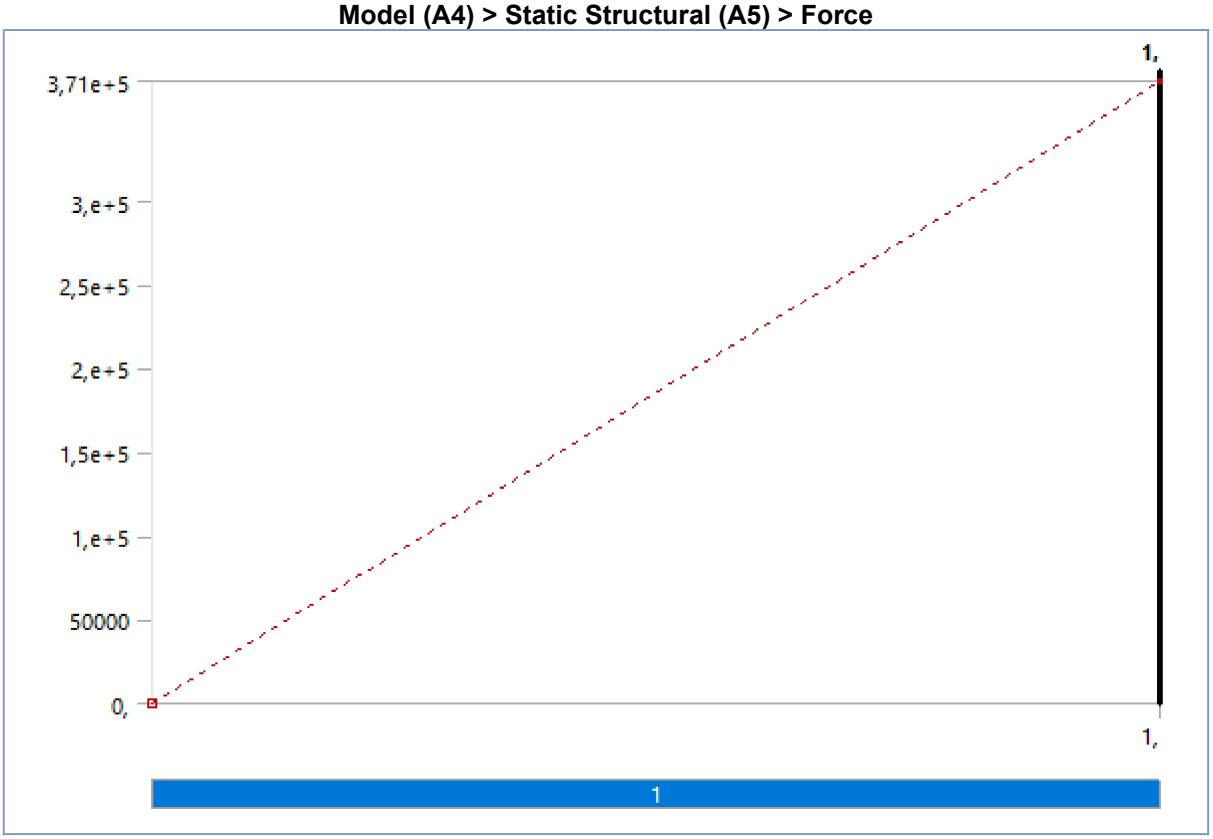

FIGURE 3
Model (A4) > Static Structural (A5) > Displacement

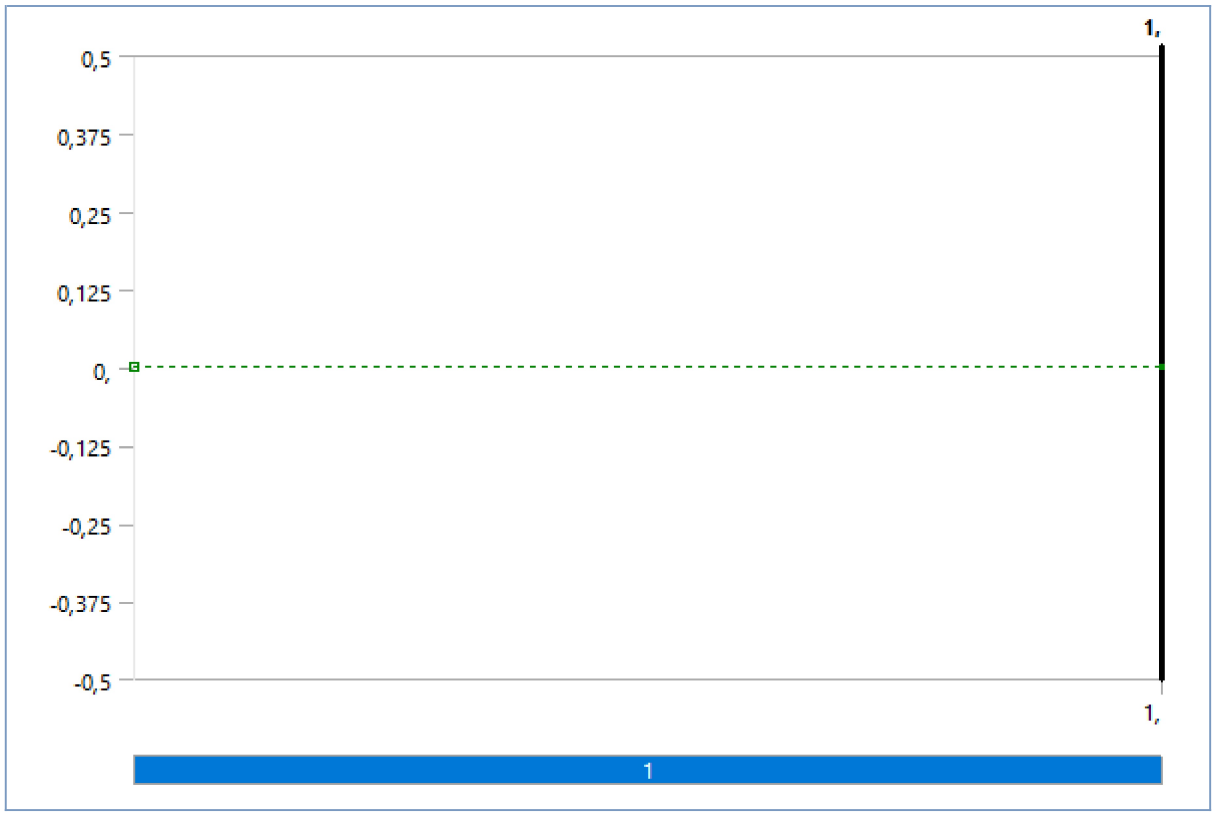

Solution (A6)

TABLE 15
Model (A4) > Static Structural (A5) > Solution

Object Name	*Solution (A6)*
State	Solved
Adaptive Mesh Refinement	
Max Refinement Loops	1,
Refinement Depth	2,
Information	
Status	Done
MAPDL Elapsed Time	9, s
MAPDL Memory Used	605, MB
MAPDL Result File Size	13,875 MB
Post Processing	
Beam Section Results	No
On Demand Stress/Strain	No

TABLE 16
Model (A4) > Static Structural (A5) > Solution (A6) > Solution Information

Object Name	*Solution Information*
State	Solved
Solution Information	
Solution Output	Solver Output
Newton-Raphson Residuals	0
Identify Element Violations	0
Update Interval	2,5 s
Display Points	All
FE Connection Visibility	
Activate Visibility	Yes
Display	All FE Connectors
Draw Connections Attached To	All Nodes

Line Color	Connection Type
Visible on Results	No
Line Thickness	Single
Display Type	Lines

TABLE 17
Model (A4) > Static Structural (A5) > Solution (A6) > Results

Object Name	*Equivalent Stress*	*Total Deformation*
State	Solved	
Scope		
Scoping Method	Geometry Selection	
Geometry	All Bodies	
Position	Top/Bottom	
Definition		
Type	Equivalent (von-Mises) Stress	Total Deformation
By	Time	
Display Time	Last	
Calculate Time History	Yes	
Identifier		
Suppressed	No	
Integration Point Results		
Display Option	Averaged	
Average Across Bodies	No	
Results		
Minimum	0, MPa	0, mm
Maximum	355,16 MPa	1,4113 mm
Average	53,632 MPa	0,65058 mm
Minimum Occurs On	Surface Body	Solid
Maximum Occurs On	Solid	
Information		
Time	1, s	
Load Step	1	
Substep	1	
Iteration Number	1	

FIGURE 4
Model (A4) > Static Structural (A5) > Solution (A6) > Equivalent Stress

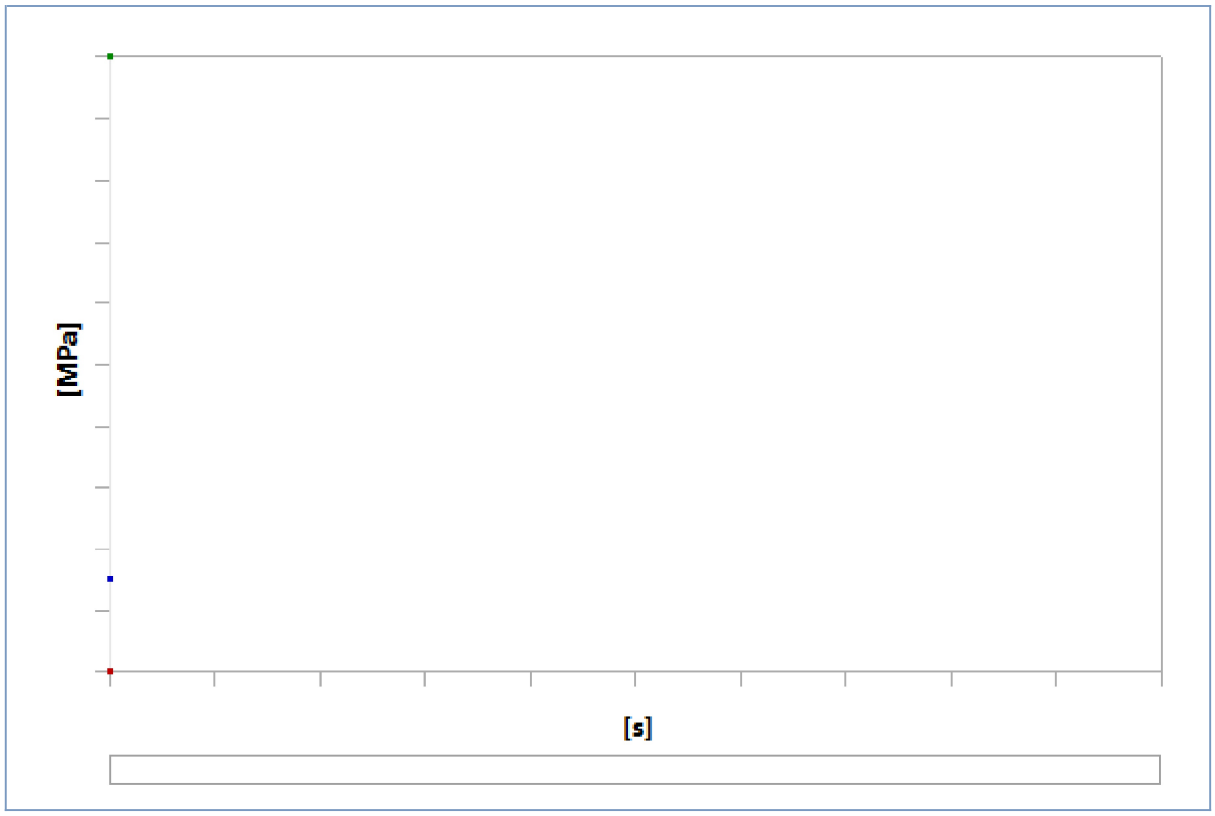

TABLE 18
Model (A4) > Static Structural (A5) > Solution (A6) > Equivalent Stress

Time [s]	Minimum [MPa]	Maximum [MPa]	Average [MPa]
1,	0,	355,16	53,632

FIGURE 5
Model (A4) > Static Structural (A5) > Solution (A6) > Equivalent Stress > Figure

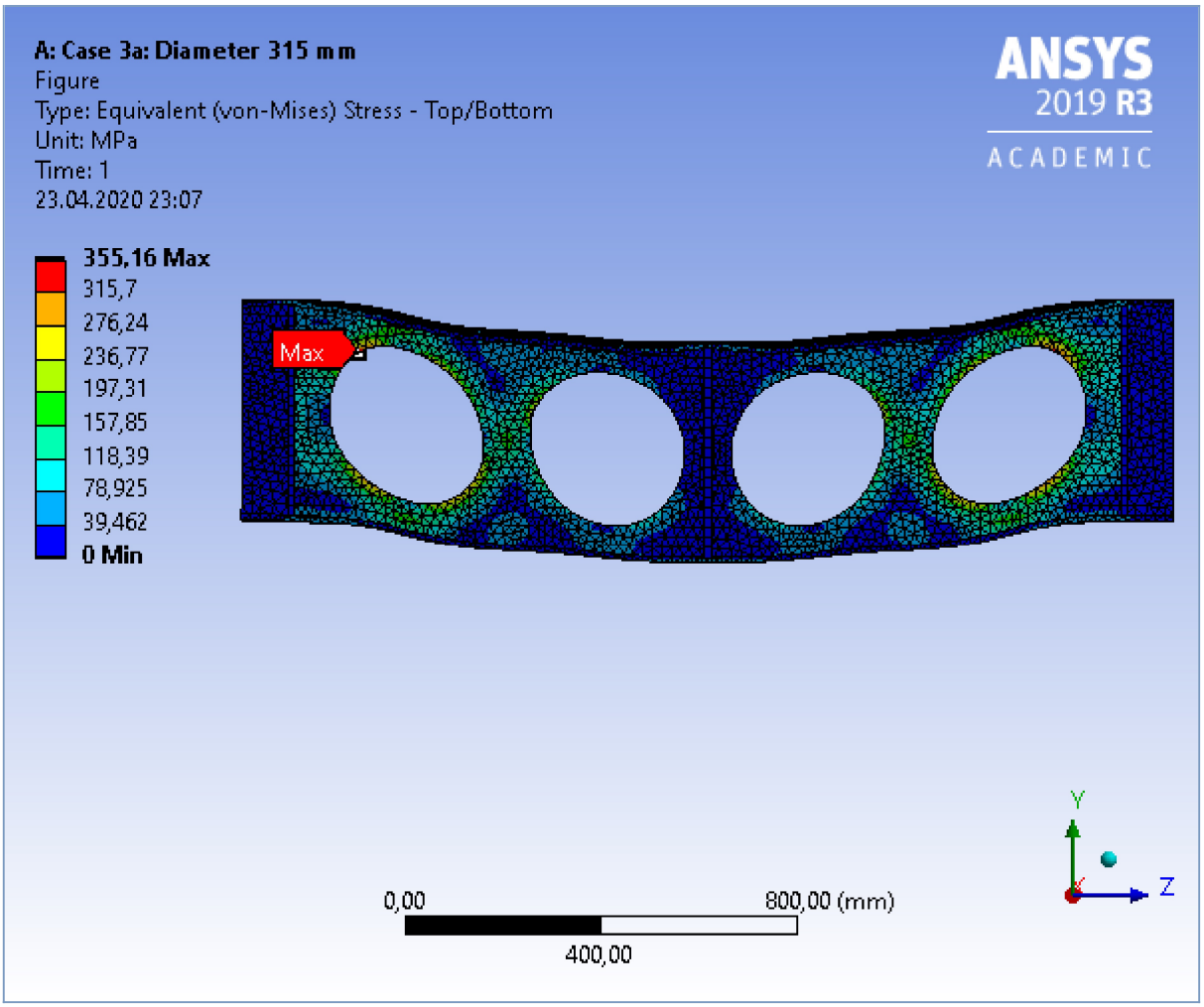

FIGURE 6
Model (A4) > Static Structural (A5) > Solution (A6) > Total Deformation

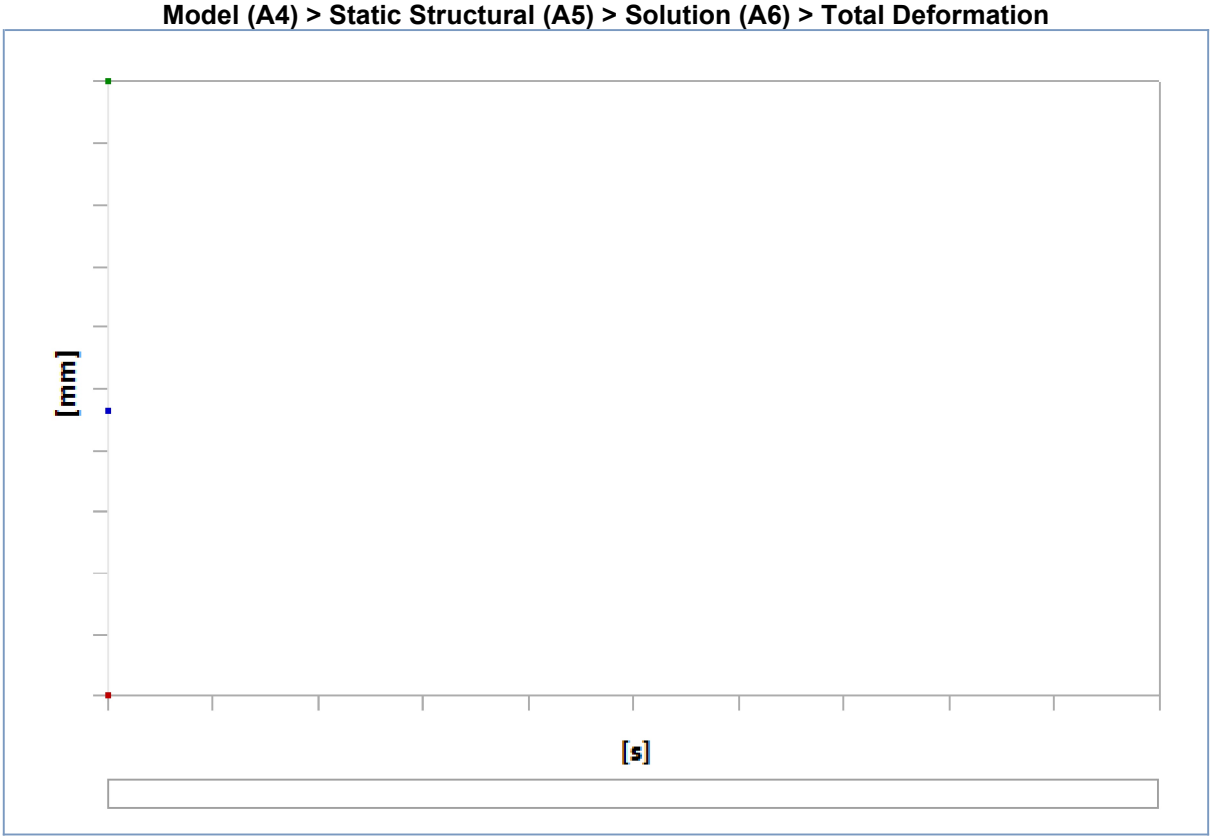

TABLE 19
Model (A4) > Static Structural (A5) > Solution (A6) > Total Deformation

Time [s]	Minimum [mm]	Maximum [mm]	Average [mm]
1,	0,	1,4113	0,65058

FIGURE 7
Model (A4) > Static Structural (A5) > Solution (A6) > Total Deformation > Figure

Material Data

Structural Steel

TABLE 20
Structural Steel > Constants

Density	7,85e-006 kg mm^-3
Coefficient of Thermal Expansion	1,2e-005 C^-1
Specific Heat	4,34e+005 mJ kg^-1 C^-1
Thermal Conductivity	6,05e-002 W mm^-1 C^-1
Resistivity	1,7e-004 ohm mm

TABLE 21
Structural Steel > Color

Red	Green	Blue
132,	139,	179,

TABLE 22
Structural Steel > Compressive Ultimate Strength

Compressive Ultimate Strength MPa
510,

TABLE 23
Structural Steel > Compressive Yield Strength

Compressive Yield Strength MPa
355,

TABLE 24
Structural Steel > Tensile Yield Strength

Tensile Yield Strength MPa
355,

TABLE 25
Structural Steel > Tensile Ultimate Strength

Tensile Ultimate Strength MPa
510,

TABLE 26
Structural Steel > Isotropic Secant Coefficient of Thermal Expansion

Zero-Thermal-Strain Reference Temperature C
22,

TABLE 27
Structural Steel > S-N Curve

Alternating Stress MPa	Cycles	Mean Stress MPa
3999,	10,	0,
2827,	20,	0,
1896,	50,	0,
1413,	100,	0,
1069,	200,	0,
441,	2000,	0,
262,	10000	0,
214,	20000	0,
138,	1,e+005	0,
114,	2,e+005	0,
86,2	1,e+006	0,

TABLE 28
Structural Steel > Strain-Life Parameters

Strength Coefficient MPa	Strength Exponent	Ductility Coefficient	Ductility Exponent	Cyclic Strength Coefficient MPa	Cyclic Strain Hardening Exponent
920,	-0,106	0,213	-0,47	1000,	0,2

TABLE 29
Structural Steel > Isotropic Elasticity

Young's Modulus MPa	Poisson's Ratio	Bulk Modulus MPa	Shear Modulus MPa	Temperature C
2,1e+005	0,3	1,75e+005	80769	

TABLE 30
Structural Steel > Isotropic Relative Permeability

Relative Permeability
10000

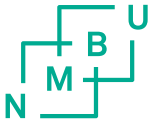

Norges miljø- og biovitenskapelige universitet
Noregs miljø- og biovitskapelege universitet
Norwegian University of Life Sciences

Postboks 5003
NO-1432 Ås
Norway